

# Assessment of Diaphragm Function during Inspiration in Pompe Disease using Static Breath-hold 3D MRI

A mesh model-based study into diaphragm impairment

by

Ricardo J.P. Juffermans

a thesis report presented to obtain the degree of

Master of Science

in BioMedical Engineering

at the Delft University of Technology

to be defended publicly on August 29, 2023

Student number: 4749758  
Course code: BM51032  
Project period: January 2022 – August 2023  
Supervisors: prof.dr.ir. Jaap Harlaar  
drs. Pierluigi Ciet  
Thesis committee: dr.ir. Nazli Tümer



# Abstract

**Background** Pompe disease is a progressive muscular disorder that will affect the respiratory muscles, in particular the diaphragm, thereby seriously limiting the respiratory function. Respiratory function is typically assessed using spirometry. However early stages of diaphragm impairment may not be detected by conventional spirometry measurements due to compensatory efforts of other inspiratory muscles. In this study we aimed to use 3D MRI as a sensitive method to assess diaphragm function and identify diaphragm impairment.

**Methods** Static breath-hold 3D MRI scans at maximal inspiration and maximal expiration were obtained from a previously used dataset in 18 healthy controls and 35 Pompe patients with varying degrees of diaphragm weakness. Images were segmented using an automatic script. The segmentations were used to create an anatomically accurate 3D mesh model of the lungs. The surface of the mesh was divided into topographical segments based on the anatomical surfaces of the lungs. Vital capacity (VC) measurements were retrieved from the mesh model ( $VC_{\text{mesh}}$ ) and compared against spirometry VC measurements made during the MRI acquisition ( $VC_{\text{spiro}}$ ) in order to validate the mesh model. Segmental volumes, derived from the topographical segments identified on the surface of the mesh model, were reallocated based on changes in lung dimensions to provide a more accurate functional topographical representation of the underlying diaphragm and intercostal muscle functions. The relative contributions of the diaphragm and intercostal muscles to the total increase in lung volume during inspiration were assessed for differences between healthy controls and Pompe patients and compared against common spirometry and 2D analysis outcomes.

**Results** A large and significant correlation was established between  $VC_{\text{mesh}}$  and  $VC_{\text{spiro}}$ ,  $r_s = 0.971$ ,  $p < 0.001$ . Median  $VC_{\text{spiro}}$  was significantly larger than median  $VC_{\text{mesh}}$  across all population groups ( $p < 0.001$ ), by an average amount of 0.31 L. This represented a mean difference between the two measurement methods of 9.3% of the mean VC measurements. It has also been demonstrated that median changes in diaphragm volume ( $p < 0.001$ ) and the median relative contribution of the diaphragm to the total increase in lung volume during inspiration ( $p = 0.009$ ) were lower in Pompe patients with decreased spirometry results when compared against healthy controls. Changes in diaphragm volumes correlated well with conventional VC and FVC measurements ( $r_s = 0.997$ ,  $p < 0.001$ ) as well as with changes in superoinferior lung sizes ( $r_s = 0.936$ ,  $p < 0.001$ ). In some Pompe patients with decreased spirometry results no indication for diaphragm impairment was found when assessing the relative contribution of the diaphragm to the total increase in lung volume during inspiration.

**Conclusion** A mesh model based on 3D MRI segmentations provides an accurate method of assessing diaphragm function. Changes in diaphragm volume and the contribution of the diaphragm to the increase in lung volume during inspiration allow for the assessment of diaphragm impairment in Pompe patients. These biomarkers of diaphragm function may prove to be highly useful in determining a personalized treatment plan for Pompe patients as well as a sensitive outcome in trials to test future treatment modalities.

# Contents

Abstract .....	i
General introduction .....	1
Chapter 1: Assessing the vital capacity of the lungs using static 3D MRI .....	6
1.1 Introduction .....	6
1.2 Methods .....	7
1.2.1 Lung mesh model generation .....	9
1.2.2 Triangle face feature labeling .....	11
1.2.2.1 Lung surface identification.....	11
1.2.2.2 Costal lung surface subdivision.....	13
1.2.2.3 Triangle face label repair.....	15
1.2.3 Defining lung volume outcomes.....	17
1.2.4 Statistical analysis .....	18
1.3 Results .....	19
1.3.1 Spirometry vital capacity measurements .....	19
1.3.2 Mesh model lung volume related outcomes .....	19
1.3.3 Level of agreement in determination of vital capacity.....	21
1.4 Discussion .....	22
1.5 Conclusion .....	24
Chapter 2: Assessing diaphragm function in patients with Pompe disease using 3D mesh model of the lungs.....	25
2.1 Introduction .....	25
2.2 Methods .....	26
2.2.1 Adjusting lung segmental allocations based on muscle functions .....	27
2.2.2 Mesh model related outcomes.....	30
2.2.2.1 Defining the diaphragm and costal segments .....	30
2.2.2.2 Lung size related outcomes .....	30
2.2.3 Statistical analysis .....	32
2.3 Results.....	33
2.3.1 Expiratory segmental volumes.....	33
2.3.2 Segmental volumes in the anatomical topographical representation.....	33
2.3.3 Segmental volumes in the functional topographical representation.....	35
2.3.4 Diaphragm and costal segment volume and contribution .....	38
2.3.5 Summed diaphragm and costal volumes and ratios .....	38
2.3.6 Comparison of mesh-derived segmental volumes to PFT outcomes.....	39
2.3.7 Superiorinferior and anteroposterior lung sizes and ratios .....	40
2.3.8 Comparison of mesh-derived segmental volumes to lung sizes and ratios .....	40
2.4 Discussion .....	42
2.5 Conclusion .....	47
General discussion.....	48
References.....	51
Appendix A – Mesh VC compared against spirometry FVC.....	55

# General introduction

## Pompe disease

Pompe disease, also known as glycogen storage disease type II, is a rare genetic autosomal disorder that affects the body's ability to break down glycogen. It is caused by a deficiency of the lysosomal enzyme acid alpha-glucosidase (GAA), which is responsible for breaking down glycogen into glucose (van den Ploeg & Reuser, 2008). In individuals with Pompe disease, the enzyme deficiency causes glycogen to accumulate in various tissues of the body, particularly in the muscles. The buildup of glycogen leads to progressive muscle weakness and can affect various key body systems, such as the heart, respiratory system and skeletal muscles. Pompe disease occurs in approximately 1 in 40.000 newborns in the Netherlands (Ausems et al., 1999), yielding in the region of 400 patients with Pompe disease. Pompe disease is typically diagnosed through clinical evaluation, genetic testing, and/or enzyme activity tests. The only current treatment for Pompe disease involves enzyme replacement therapy (ERT), which aims to provide the missing or deficient enzyme to the body. ERT is, however, not a cure for Pompe disease, though it can help manage the symptoms and slow down the progression of the disease hereby increasing life-expectancy. ERT is typically introduced once the first symptoms specific to Pompe disease are starting to appear (Barba-Romero et al., 2012; Stockton et al., 2020).

There are two forms of Pompe disease: infantile-onset and late-onset. Infantile-onset Pompe disease is the most severe form and typically presents within the first few months after birth. Babies with this form of the disease experience muscle weakness, an enlarged heart and breathing difficulties. Without treatment it can lead to severe disability and early death. Even with treatment patients with infantile-onset Pompe disease rarely survive for longer than 12 months (van den Hout et al., 2003). Late-onset Pompe disease is milder and can manifest anytime from childhood to adulthood. This form primarily affects the muscles, causing progressive muscle weakness. Typical symptoms include fatigue, difficulty climbing stairs, and problems with swallowing and speaking. As the disease progresses and starts to affect the respiratory muscles patients will start to encounter respiratory difficulties and dysfunction. Weakness of the diaphragm is generally considered to be the leading cause behind the decreased respiratory function often encountered by patients with Pompe disease (Pellegrini et al., 2005).

## Respiratory muscles

The primary muscles involved in respiration are the diaphragm and the (external and internal) intercostal muscles. The diaphragm is the main respiratory muscle responsible for inspiration. It is a dome-shaped muscle located at the base of the lungs (Figure 1) and separates the chest cavity from the abdominal cavity. During inhalation the diaphragm contracts, hereby moving downwards as it flattens. This movement subsequently increases the volume of the thoracic cavity which allows the lungs to expand and fill with air (De Troyer & Boriek, 2011).

The intercostal muscles are positioned between the ribs. There are two types of intercostal muscles: external intercostal muscles and internal intercostal muscles.. Second to the diaphragm, the external intercostal muscles also aid during inspiration. Together they are the main driving force behind inspiration (McCool & Tzelepis, 2012). By pulling the ribs



**Figure 1.** A representation of the positioning, orientation and dome shape of the diaphragm.

upward and outward, the external intercostal muscles expand the thoracic cavity during inspiration which allows the lungs to fill with air. The internal intercostal muscles on the other hand are active during forced exhalation and aid in reducing the volume of the thoracic cavity by pulling the ribs downward and inward. Additionally there are several other accessory respiratory muscles that can assist during the process of respiration when needed. Some examples include the sternocleidomastoid, scalene muscles and the abdominal muscles (De Troyer & Boriek, 2011).

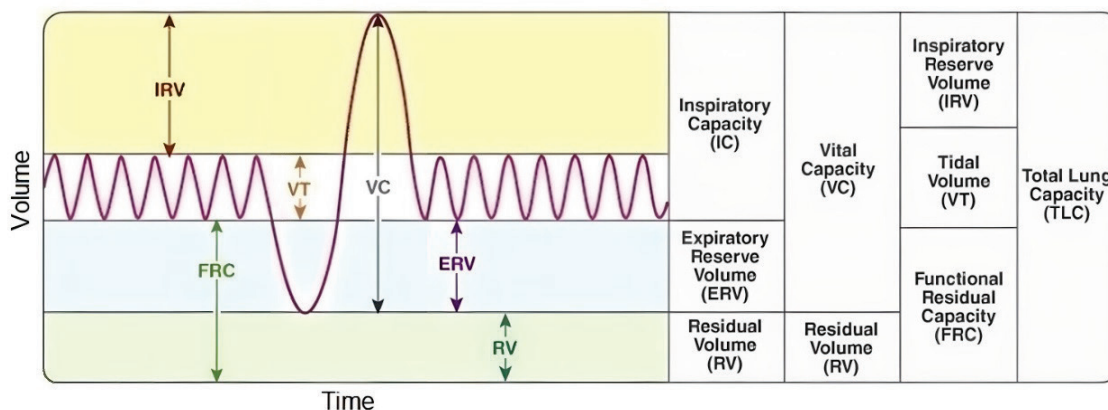


**Figure 2.** A representation of lung volumes and lung capacities during respiration. The figure depicts a regular (quiet) breathing pattern interrupted by a maximal expiration which is immediately followed by a maximal (forced) inspiration maneuver.

### Assessment of respiratory function

Respiratory function is typically assessed using a pulmonary function test (PFT). PFTs are conventionally used with both healthy individuals and patients with a respiratory disease. A PFT can be composed of two types of tests: spirometry and body plethysmography. Body plethysmography tests are infrequently used to assess respiratory function and are mainly used to determine absolute lung values (Criée et al., 2011), such as the total lung capacity (TLC) and residual volume (RV). An overview of lung volumes and capacities is shown in Figure 2. Spirometry is the most used type of PFT and the gold standard when it comes to assessing respiratory function (Graham et al., 2019). It is performed by forcefully breathing in or out through the mouth into a spirometer, a device that contains a flowmeter, in order to measure the airflow in and out of the lungs as a function of time. Measurements of the airflow are important when assessing global lung function (Barreiro & Perillo, 2004). The most commonly measured variables relating to the airflow are the vital capacity, forced vital capacity and the forced expiratory & inspiratory volumes (see Figures 2 & 3). The vital capacity (VC) measures the volume of air exhaled or inhaled during a regular breath. The forced vital capacity (FVC) measures the volume of air forcefully exhaled during a forced breathing maneuver, a maneuver where one exhales as much air as one can after taking a deep breath. FVC is often measured in either an upright or a supine position. The difference in FVC between these two measurements ( $\Delta$ FVC, also known as the supine FVC drop or postural drop) can provide an indication of diaphragm weakness.

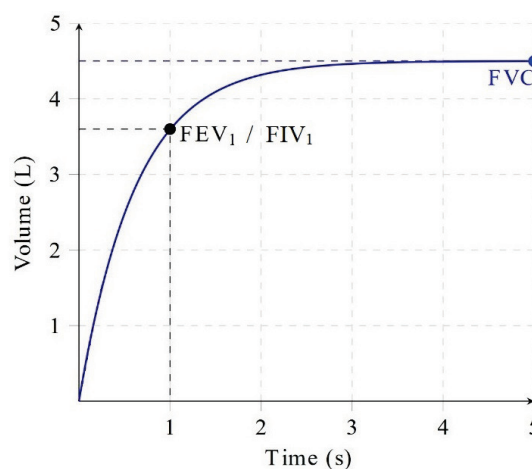


**Figure 3.** Measurement of change in volume over time (flow) during a spirometry test.

In healthy individuals the FVC is typically between 3% and 8% lower in the supine position than in an upright position. A postural drop larger than 20-25% is customarily seen as an indication of diaphragm weakness (Fromageot et al. 2001). The forced expiratory volume ( $FEV_1$ ), also measured during a forced breathing maneuver, measures the volume of air forcefully exhaled in the first second of the forced breathing maneuver. A spirometry test can alternatively also be performed during a forced inspiratory maneuver by inhaling as much as one can after a maximal exhalation. This also allows for FVC to be measured alongside the forced inspiratory volume ( $FIV_1$ ). An overview of the measurements of FVC and  $FEV_1/FIV_1$  during a typical forced expiratory or inspiratory maneuver is depicted in Figure 3.

### Assessment of diaphragm function with a PFT in patients with Pompe disease

Spirometry measurements (and other PFTs in general) are powerful and invaluable tools for clinicians that can aid in the detection, diagnosis, management and treatment of diseases such as COPD (Johns et al., 2014) and asthma (Celli, 2000). When assessing the function of the diaphragm however, a spirometry measurement is less useful as it only provides information about the global (or net) respiratory function. While spirometry can provide an indication of diaphragm weakness by assessment of the postural drop, it cannot otherwise be used to assess diaphragm function directly.

In patients with Pompe disease an impairment of the diaphragm may not be noticed during a regular spirometry test due to compensatory efforts of other (accessory) respiratory muscles. These compensatory efforts are fairly common in the early stages of respiratory dysfunction and can therefore mask early loss of diaphragm function (Parthasarathy et al., 2007). With diaphragm weakness being an important biomarker in identifying the development of Pompe disease, the progression of the disease may not be portrayed accurately. Early and accurate identification of diaphragm weakness is essential in formulating a treatment plan for patients with Pompe disease and may allow for the ERT to start earlier, hereby potentially increasing the efficacy of the treatment program (Cupler et al., 2012; Schneider et al., 2013; Stockton et al., 2020). There is therefore a strong need for a better way to assess the function of the respiratory muscles, in particular the diaphragm.

### Assessment of diaphragm function by imaging methods

Previous research has shown imaging methods to be a promising method for assessing the function of key components of the respiratory system. Various studies have made use of 2D magnetic resonance imaging (MRI) to evaluate the motion and mechanics of the lungs by assessing changes in the dimension of the thoracic cavity, lung area and diaphragm curvature (Figure 4; Gaeta et al., 2015; Harlaar et al., 2021; Harlaar et al., 2022). These outcomes are generally computed at the level of the right hemidiaphragm. Analysis on the left side of the lung is complicated in 2D analysis due to the positioning of the heart and surrounding structures. The segmentation of the 2D images and subsequent analysis of the segmentations is relatively straightforward as they only have to be performed on a single slice of the MRI data.

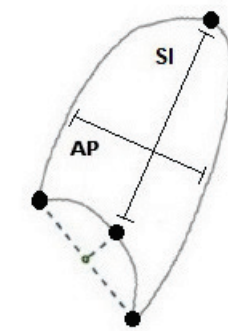


**Figure 4.** A 2D representation of the superoinferior (SI) and antero-posterior (AP) lung sizes.

In recent years 3D MRI and computed tomography (CT) have also seen use in evaluating respiratory muscle functions, mainly in assessing (trunk) muscle involvement (MRI: Alejaldre et al., 2012; Carlier et al., 2012; Figueroa-Bonaparte et al., 2016; Gaeta et al., 2013; Wens et al., 2015 & CT: Alejaldre et al., 2012; Gaeta et al., 2013), but also in assessing lung volumes

(MRI: Mogalle et al., 2016; CT: Bakker et al., 2022). Although CT scans are generally easier to perform on patients and acquisition times for CT are normally shorter than for MRI (especially for 3D acquisitions), MRI performs much better when used to generate images of soft-tissue structures such as the lungs, providing a better resolution and higher level of detail while also not making use of ionizing radiation. Another technique that has recently seen more use in assessing the diaphragm is ultrasound imaging. A recent study demonstrated that the thickness of the diaphragm was reduced in Pompe patients (Ruggeri et al., 2020). This finding correlated well with spirometry measurements. However, ultrasound imaging cannot easily be used to compare simultaneous movements of the diaphragm and intercostal muscles during inspiration. For all these reasons MRI is therefore, when possible, the preferred method when assessing lung mechanics.

When used for assessing respiratory function 3D MRI has the advantage over 2D MRI that it can readily be used to assess lung volumes directly, while 2D MRI can only be used to assess the lung area over a single slice as an indication of the lung volume. Another key advantage over 2D MRI is that analysis of 3D MRI can provide a larger number of potential parameters that can be assessed in the post-processing. As an example the slice obtained during 2D MRI, which is typically made in the sagittal plane to allow for analysis of the anteroposterior dimensions changes, cannot be used to assess for parameters in the medio-lateral direction. These parameters are key aspects of respiratory mechanics given that the lungs expand not only in the anterior direction, but also in the lateral direction when the external intercostal muscles contract. Furthermore, analysis of 2D MRI images typically requires the acquisition of multiple separate 2D images in order to cover the entire region of interest. A single 3D MRI scan may therefore actually have a lower overall acquisition time than multiple separate 2D images of individual slices (Shirly & Ramesh, 2019; Walter et al., 2023). Lastly, an individual is required to lay still for a comparatively long time during the MRI acquisition. When assessing multiple 2D slices obtained in succession the orientation of the structures of interest may have slightly shifted in between acquisitions due to movements of the individual.

### **Using 3D MRI to create a mesh model of the lungs**

One approach for assessing respiratory function using 3D MRI data is by making use of a three-dimensional mesh model of the lungs (Mogalle et al., 2016). A mesh model is a three-dimensional representation of an object or surface created using a polygon mesh structure and is composed of interconnected vertices, edges, and faces that define and represent the geometry of the object or surface. Once generated the mesh structure describing the mesh model is lightweight, efficient and easily accessible for further processing. Mesh models are widely used in various fields, including medical imaging (Archip et al., 2006; Levine et al., 2012) for visualization, rendering, simulation and various other analytic purposes. Mesh models are very suitable for modelling complex shapes due to their high versatility. This includes deformable soft tissues as the lungs and its surrounding structures. The use of a mesh model allows for identification of subtle and intricate details in the texture of the surface such as smooth curves and hard edges. This is particularly convenient when analyzing the lung surface as it contains both highly convex and concave regions. Additionally, a mesh model should allow for the identification of the surface of the diaphragm on the lung surface. Using multiple 3D MRI scans at different stages of the respiratory cycle, changes in shape and positioning of the diaphragm during inspiration can be analyzed. Detailed assessment of these parameters should allow us to specifically address the function of the diaphragm.

### **Research questions**

This report covers two main research questions. Each research question is addressed in a separate chapter. In Chapter 1 we aim to design and evaluate an anatomically correct mesh model of the lungs capable of assessing lung volume changes based on static breath-hold 3D MRI images at maximal inspiration and maximal expiration. In Chapter 2 we aim use the meshes generated using the method described in Chapter 1 to quantify the function of the diaphragm in patients with Pompe disease by examining the contribution of the diaphragm to volume changes during inspiration.

# Chapter 1: Assessing the vital capacity of the lungs using static 3D MRI

## 1.1 Introduction

The main goal in this study is to assess diaphragm function during inspiration. A conventional PFT cannot be used to assess diaphragm function as it only provides information about the global respiratory function. An alternative means of assessing respiratory function directly is to make use of an imaging method such as 3D MRI to examine key aspects of the lung mechanics. The position and orientation of the lungs can be readily retrieved by segmenting images obtained using 3D MRI. This data can be used to generate a mesh model of the lungs which allows for detailed analysis of the lung surfaces and volumes. The main objective of this chapter was to investigate whether we could design an anatomically accurate three-dimensional mesh model of the lungs using static breath-hold 3D MRI images at maximal inspiration and maximal expiration, and evaluate the accuracy of the mesh model in assessing the vital capacity of the lungs by comparing against spirometry results.

### 1.2 Methods

#### Data acquisition and study population

The dataset used in this chapter was obtained from measurements made in a previous study (Harlaar et al., 2021). The dataset contains static breath-hold 3D MRI scans for both maximal inspiration and maximal expiration conditions in 53 participants. Of the 53 participants, 35 were patients with Pompe disease and 18 were healthy age and sex matched controls. Segmentations of each lung in the dataset had been generated from the MRI scans using a deep-learning based algorithm and were processed by experienced analysts. An example of a 3D segmentation is shown in Figure 5. Spirometry data was collected prior to the MRI acquisition in both an upright and supine position ( $FVC_{\text{upright}}$  &  $FVC_{\text{supine}}$ ) as well as during the MRI acquisition in the supine position ( $VC_{\text{spiro}}$ ). Like in the original study from Harlaar et al. (2021) the patients with Pompe disease were subdivided into two subgroups based on their  $FVC_{\text{supine}}$  measurements. In one group patients ( $N = 13$ ) presented with normal spirometry results ( $FVC_{\text{supine}}$  was  $\geq 80\%$  of the predicted value and had a z-score  $\geq -1.64$ ), while the patients in the other group ( $N = 22$ ) presented with decreased spirometry results ( $FVC_{\text{supine}}$  was  $< 80\%$  of the predicted value or had a z-score  $< -1.64$ ).

#### Data processing

All mesh generation and feature labeling algorithms described below have been implemented in Python (Python release 3.9) using the integrated development environment (IDE) PyCharm Community Edition (version 2022.1). The MRI data was loaded in to Python using the Nibabel library (version 4.0.1) and mesh structures were visualized using the interactive graphing library Plotly (version 5.15.0).

#### Textbox 1: Anatomical lung surfaces

The surface of the mesh, describing the surface of the lung, is divided into segments based on the anatomical depiction of the lung surface. The lung surface is anatomically divided into three distinctly different surfaces: the costal, medial and diaphragmatic surfaces (Figure 6). The costal surface of the lung has the largest surface area and covers the region of the lung surface where the lung is connected to the chest walls by the pulmonary pleurae (Chaudhry & Bordonni, 2022). It is a mostly convex surface, except for the narrow indentations on the lung surface where the ribs are positioned. The medial surface of the lung covers the region separating the lung surface from the thoracic and spinal cavities. It can be further divided into an anterior region; the mediastinal surface and an posterior region; the vertebral surface. The medial surface is an intrinsically concave surface due to its positioning directly adjacent to the spinal cord, the heart and various major veins and arteries. The diaphragmatic surface of the lung covers the region of the lung surface that rests on top of the convex dome surface of the diaphragm and is, like the medial surface, a concave surface. The diaphragmatic surface is connected to the costal surface via the inferior border, also defined as the costal line of pleural reflection. This border is typically clearly defined by a fairly abrupt change in the curvature of the lung surface. The costal surface is connected to the mediastinal surface via the anterior and posterior borders. The anterior border coincides with the sternal line of pleural reflection and is typically also clearly defined due to an abrupt change in curvature. The posterior border on the other hand coincides with the vertebral line of pleural reflection and is less clearly defined as the change in curvature of the lung surface at this point is fairly smooth, thereby giving the posterior border a more rounded edge. Lastly, the boundary between the medial and the diaphragmatic surface is often ill-defined due to the concave natures of both surfaces and the large inter-subject variability in the exact positioning of the structures in the thoracic cavity (e.g. the heart).

## 1.2 Methods

The pipeline in which the mesh generation and feature labeling is performed is largely based on the previous work of Mogalle et al. (2016), originally implemented in Matlab. Various functions provided by the iso2mesh toolbox (Fang & Boas, 2009; Tran et al., 2020) were used by Mogalle et al. for the realization of the pipeline. As this toolbox is not readily available in Python, multiple functions provided by the toolbox have been adapted and rewritten to be implemented in Python.

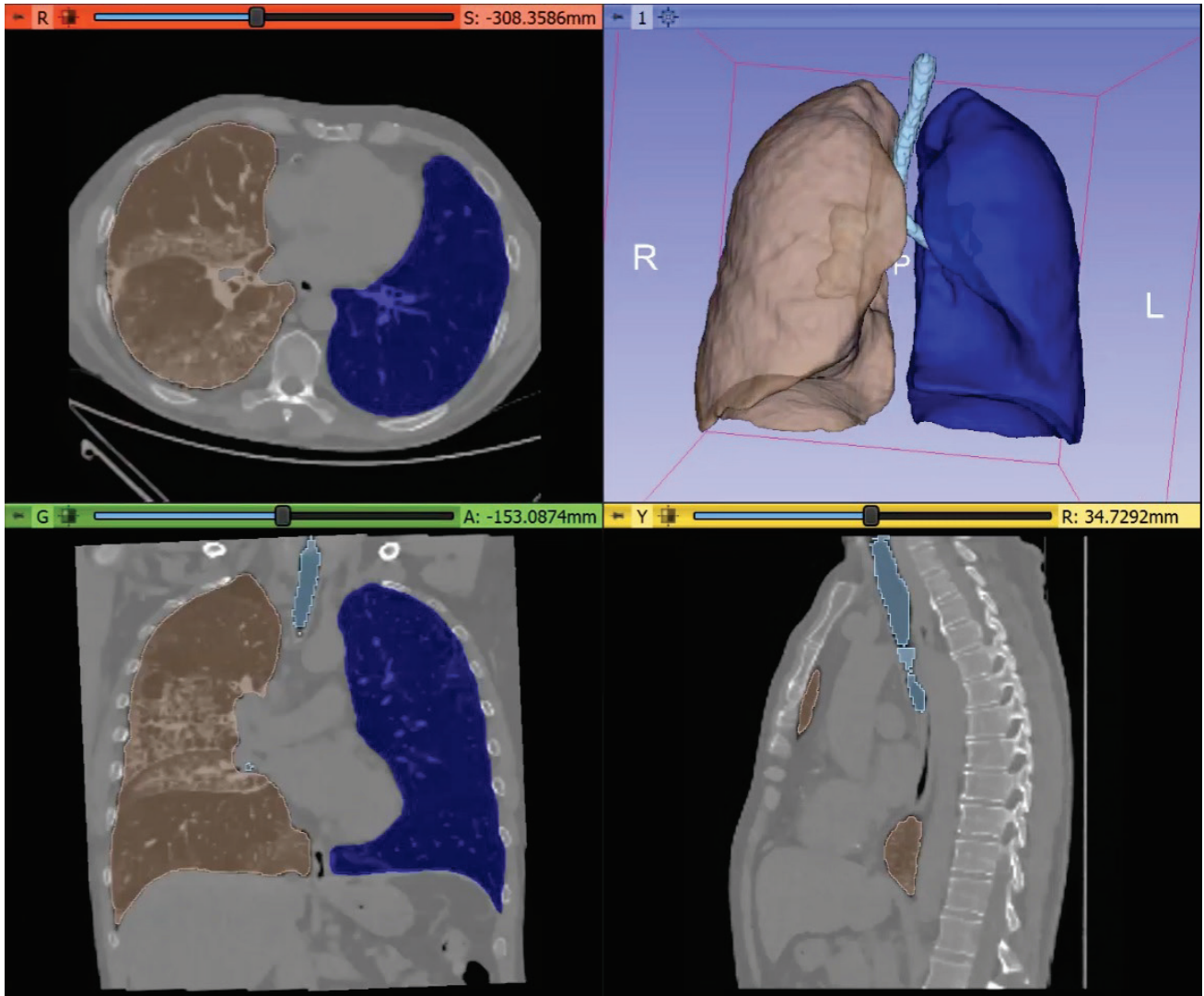


**Figure 5.** A two-dimensional slice of the lungs is shown in the transverse (top-left), coronal (bottom-left) and sagittal (bottom-right) planes. For each slice the image is partitioned by assigning a label to every pixel that belongs to a particular region (e.g. either the left or right side of the lungs). The labels are combined for each slice in every plane to generate the three-dimensional segmentation of the lungs (top-right).

### 1.2.1 Lung mesh model generation

A mesh structure was generated from the MRI segmentations using a Delaunay refinement algorithm provided by the Pygalmesh software (version 0.10.6). Pygalmesh is a Python frontend program based on the mesh generation capabilities provided by the Computational Geometry Algorithms Library (CGAL) and is freely available under the GNU General Public License (GPL). The generated mesh structure consists of a set of nodes  $\mathbf{N}$  and a set of triangle faces  $\mathbf{F}$ . The set of nodes describes the location in three-dimensional space of all vertices embedded within the mesh structure. Each triangle face in the set of triangle faces  $\mathbf{F}$  contains the index number of three nodes out of the set of nodes  $\mathbf{N}$ . These nodes are connected to each other via straight line segments. These line segments make up the edges of the triangle faces. The edges define the boundaries of the individual triangle faces. Together the set of triangle faces  $\mathbf{F}$  makes up the surface of the mesh structure. A detailed depiction of these elements on the mesh surface is shown in Figure 7. For the generation of the mesh structure every voxel represents a volume of  $1 \text{ mm}^3$  (dimensions of  $1 \text{ mm} \times 1 \text{ mm} \times 1 \text{ mm}$ ). Both the maximal distance between nodes and the maximal radius of every Delaunay sphere were set to be 2 voxels. Additionally the minimal angle in a triangle face was set to be at least 30 degrees in order to prevent for triangle faces to be generated with overly acute angles.

In order to allow for further processing the mesh structure is required to be a manifold structure. The mesh structure cannot contain any holes or missing triangle faces and every edge between adjacent triangle faces must be connected to exactly two faces. Any such inconsistency in the mesh structure is referred to as a topological singularity. The mesh is assessed for the occurrence of any topological singularities. If any are present in the mesh, a cut-and-stitch algorithm is applied in order to convert the surface of the mesh structure to a manifold structure. This cut-and-stitch algorithm consists of the local cutting method and pinching stitch strategy described in the paper by Guézic et al. (2001). The mesh structure is also assessed for the orientation of the triangle faces. If necessary the structure is adjusted to ensure that the triangle faces are oriented such that the computed normal vectors are pointing outward for all triangle faces. The MeshFix algorithm (Attene, 2010) is applied to the mesh structure in order to eliminate any remaining intersections in the mesh. Afterwards the mesh is simplified by halving the number of nodes in the mesh structure using the Triangulated Surface Mesh Simplification algorithm provided by CGAL (Cacciola et al., n.d.). This algorithm makes use of the Lindstrom-Turk Cost and Placement strategy to determine which nodes need to be collapsed and repositioned in order simplify the mesh while changing the overall structure of the mesh as little as possible (Lindstrom & Turk, 1998; Lindstrom & Turk, 1999). Lastly, once all other modifications are finished, the surface of the mesh is smoothed by performing 8 iterations of a LowPass mesh surface smoothing algorithm (or LowPass filter) originally provided by the iso2mesh toolbox. The LowPass filter is based on a set of Laplacian smoothing algorithms (Bade et al., 2006; Taubin, 1995). During every iteration the Laplacian smoothing algorithms, described in Equations 1 & 2, are applied

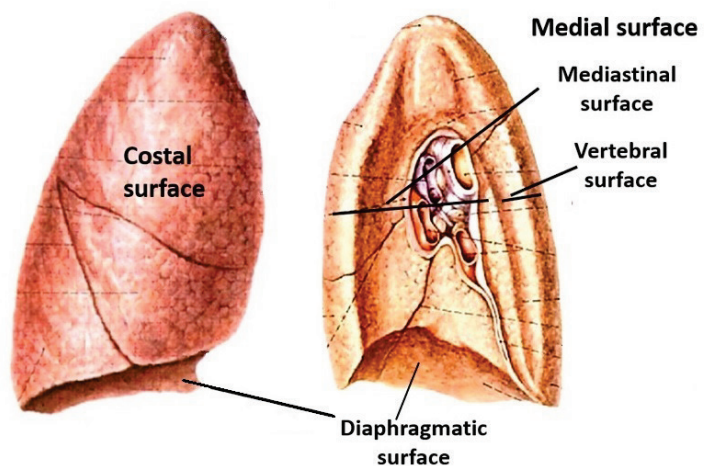


**Figure 6.** The costal, medial and diaphragmatic surfaces of the lung are depicted on the right side of the lung.

## 1.2 Methods

---

consecutively. The new positions of the nodes  $\mathbf{N}'$  are calculated based on the position of the current node and the average position of the neighboring nodes  $\mathbf{N}_{neigh}$ .

$$\mathbf{N}' = \alpha' \mathbf{N} + \frac{\alpha}{n} \sum_{i=0}^{n-1} \mathbf{N}_{neigh} \quad (1)$$

$$\mathbf{N}' = \beta' \mathbf{N} + \frac{\beta}{n} \sum_{i=0}^{n-1} \mathbf{N}_{neigh} \quad (2)$$

The result of the smoothing algorithm is dependent on various weighting factors. In Equations 1 & 2  $\alpha'$  is set to  $\alpha' = 1 - \alpha$ ,  $\beta$  is set to  $\beta = -1.02\alpha$  and  $\beta'$  is set to  $\beta' = 1 - \beta$ . As primary input to the LowPass filter  $\alpha$  is, in this particular instance, set to be equal to 1.

### 1.2.2 Triangle face feature labeling

As the main goal of this project is to assess diaphragm function by examining the contribution of the diaphragm to the increase in lung volume during inspiration, several key features of the lungs and its surrounding structures need to be identified in the mesh model. This can be achieved by assigning a feature label to every triangle face in the mesh structure in order to obtain a set of feature labels  $L$ . Every group of feature labels describes which corresponding group of triangle faces in the set of triangle faces  $F$  is associated with a particular key feature of the lungs and surrounding structures. The first step in assigning the feature labels is to distinguish between the convex and non-convex (or concave) segments in the mesh model such that we can identify the costal, medial and diaphragmatic surfaces of the lung (see Textbox 1).

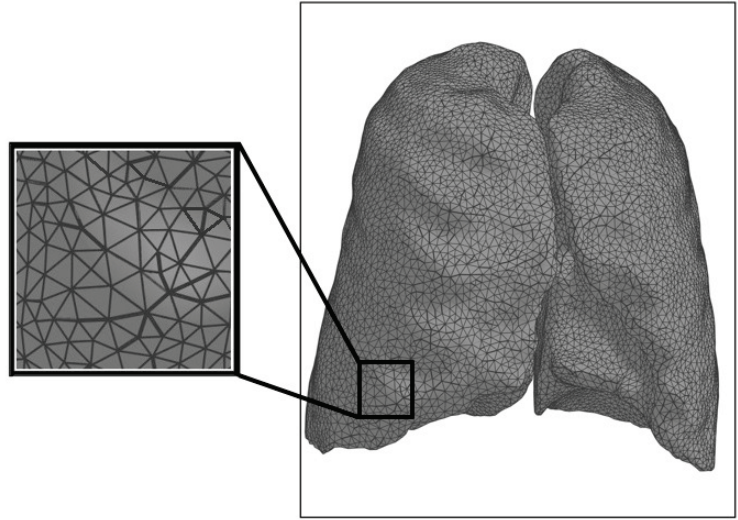


**Figure 7.** A mesh model depicting the surface of the lungs. A highlighted subsection illustrates that the surface consists of a large number of triangle faces (in grey). Each triangle face contains three nodes which are linked together by the edges (shown as black lines).

#### 1.2.2.1 Lung surface identification

In order to determine the positioning of the costal, medial and diaphragmatic surfaces in the mesh the first step in the current pipeline is to apply a watershed algorithm to the generated mesh structure. The watershed algorithm is used to divide the surface of the mesh in subsections, where the immediate surrounding area of all nodes contained within each subsection has a relatively uniform level of curvature. The subsections are separated from each other by a border of ridge nodes. Ridge nodes are nodes for which the surrounding area has large differences in curvature and they therefore do not belong to any of the subsections. Small subsections containing less than 100 nodes are removed from the set of subsections. Concave nodes are identified by calculating the minimum point to plane distance to nodes located on the convex hull of the mesh structure for all nodes in the mesh structure. All nodes for which the calculated point to plane distance is less than 12 mm are designated as concave nodes. The subsections generated by the watershed algorithm are labeled as a concave subsection if at least 20 percent of the nodes in the subsection are designated as concave nodes. The entire concave surface region, containing both the medial and diaphragmatic surfaces, is made up of all remaining concave subsections. The remaining unassigned triangle faces are all deemed to belong to the convex surface region. An example of the distinction between convex and concave regions is shown in Figure 8a.

Having identified the concave lung surface regions in the mesh model, a distinction still has to be made between the medial and diaphragmatic sections of the lung surface. Mogalle et al. (2016) achieved this by making use of a random walker algorithm. The implementation of the random walker is a variation of the random walker strategy first proposed by Grady (2006). The implementation of this strategy makes use of the concave subsections discussed in the previous paragraphs and is briefly described in the following paragraphs.

## 1.2 Methods

The initial segments for the diaphragmatic and medial surface regions are made up of a (concave) subsection which, based on the anatomical location, is the most likely subsection to be a part of the respective segments. The concave subsection that is most posteriorly and inferiorly positioned is deemed to be part of the initial diaphragmatic segment, while the most superiorly positioned concave subsection is deemed to be part of the initial medial segment. A ray tracing algorithm is then used to determine which concave subsections are ‘visible’ from a central point located at the level of the most inferior part of the lung. All concave subsections for which no more than half of the nodes in the subsection are visible from the central point are also deemed to be part of the medial segment.

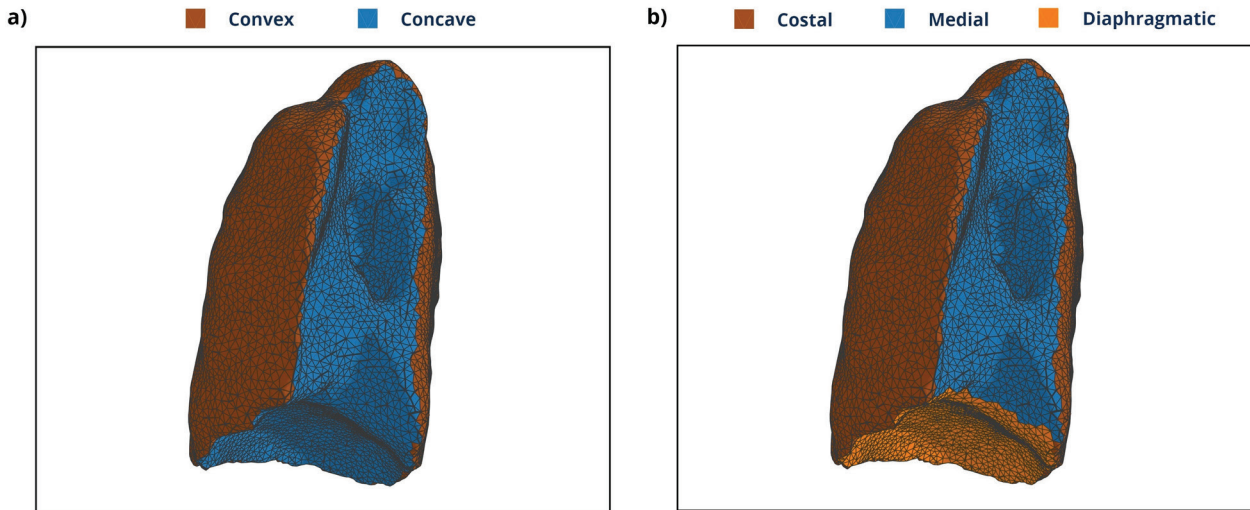


**Figure 8.** The initial lung surface identification is shown on the mesh model of the lungs. For both meshes the right side of the lungs of a healthy control is depicted in the same orientation. A) The initial mesh model with the convex and concave regions identified. B) The anatomical lung surfaces as identified on the surface of the mesh model.

The remaining unassigned concave subsections are subsequently merged one-by-one with other concave subsections according to the same cost function as used in Mogalle et al. (2016), which is based on the constrained random walker algorithm described in Zhang et al. (2010). This cost function involves several parameters; an isophotic metric and the average curvature of the normals at the center of the subsections. The isophotic metric (Potmann et al., 2004) takes into account the Euclidian distance between the centers of the subsections and the orientation of the normals of the respective subsections. The cost function is applied to all adjacent subsection pairs. In every iteration the pair with the lowest merge cost is chosen to be merged. Pairs are only allowed to merge if the output of the cost function is sufficiently low enough and either the difference in the orientation of the mean normal between subsection pairs is smaller than 20 degrees or the orientation of the normal vectors at the centers of the subsections point to the same half-space. Any remaining unassigned subsections will be assigned during the random walk.

The random walk algorithm iteratively assigns triangle faces in the remaining unassigned subsections to either medial or diaphragmatic regions until all triangle faces have been assigned and predetermined conditions have been met. Prior to the first iteration the initial starting positions of the random walk algorithm first have to be determined, these starting positions are known as seed points. The initial seed points are set as the center of the subsection for each of the original concave subsections generated by the watershed algorithm. Using the initial seeds points, the currently assigned feature labels, and the aforementioned cost function a Dirichlet problem is solved in order to obtain a probability graph that depicts the likelihood

that a triangle face is part of either the diaphragmatic or medial surface region. Triangle faces are deemed to belong to the diaphragmatic surface region if the probability of them belonging to that region is larger than 80%, while they are deemed to belong to the medial surface region if the probability of them belonging to that region is larger than 60%. At the end of the current iteration new random seed points are added as input of the random walker and a new iteration is started.

The random walker algorithm is terminated when the number of triangles faces in either the diaphragmatic or medial surface region has not changed substantially (i.e. less than 3% difference) or when both surface regions contain less triangle faces than in the previous iteration. After completion of the algorithm all triangle faces that belong to the diaphragmatic surface region with a probability percentage larger than 80% are assigned a diaphragmatic feature label. The remaining unassigned triangle faces in the concave lung surface region are assigned a medial feature label. An example of the resulting mesh label distribution is displayed in Figure 8b.

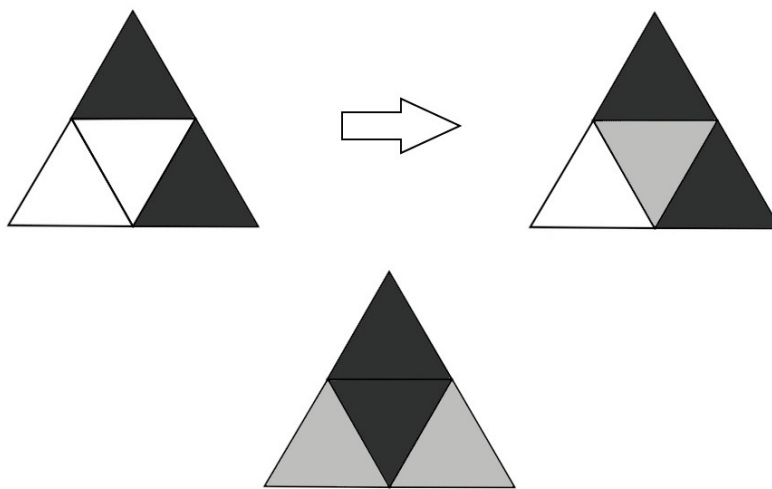


**Figure 9.** The top row depicts the labeling process during the propagation algorithm (stage 5 of the ruleset described in section 1.2.2.2). The propagation algorithm is based on the bounding box projection (depicted in the bottom row) instead of actual adjacent feature labels. The white triangle faces depict unassigned labels, while the different grey triangle faces represent distinctly different arbitrarily assigned labels.

### 1.2.2.2 Costal lung surface subdivision

Using the watershed and random walker algorithms described in the previous paragraphs the costal, medial and diaphragmatic lung surfaces have been identified. In order to allow for more detailed assessment of the costal lung surface and to increase the versatility of the mesh model, the costal lung surface is further subdivided into an anterior, posterior, lateral and superior region. The general principle used to achieve this is based on the intersection of the projected normals for each triangle face of the convex region with the bounding box of the lung. In order to obtain an accurate estimation of the bounding box intersections when comparing across participants, the orientation of the lungs has to be consistent in all participants. The orientation of the lungs is determined by computing the convex hull of the lung in the sagittal plane. The obtained outline of the lung is interpolated between the most posteriorly and inferiorly positioned point of the convex hull and the most anteriorly positioned point of the convex hull. An ellipse is then fitted over the interpolated section of the outline. The orientation of the lung is defined as the difference in angle between the principal axis of the fitted ellipse and the vertical axis of the global coordinate system. The position described by the nodes in the mesh structure is shifted by applying a rotation matrix such that the

## 1.2 Methods

---

orientation of the lung aligns with the vertical axis of the global coordinate system. When the costal subdivision algorithm has finished assigning all feature labels to the costal surface region, the mesh structure is rotated back to its original position based on the average orientation of both sides of the lungs.

Two distinct bounding boxes are used during the feature labeling; a minimal bounding box and an extended bounding box. The minimal bounding box encapsulates only one side of the lung while the extended bounding box encapsulating both sides of the lung. For both bounding boxes the bounding box projection (BBP) is obtained by projecting the normals of all triangle faces through the bounding box. Having established the BBPs the feature labels are assigned using the following ruleset for each lung separately:

- 1) Feature labels are first assigned to all convex (anterior, posterior, superior and lateral) regions in the minimal BBP. For each label only the region with largest connecting area is retained.
- 2) Feature labels are assigned to all concave (diaphragmatic and medial) regions. The diaphragmatic surface region from the random walker is retained. Feature labels for the medial surface region are only assigned to triangle faces in the medial surface region obtained from the random walker if those faces also project to the medial surface region in the minimal BBP. Any remaining non-labeled triangle faces from the original random walker medial surface region are assigned a temporary undefined label to allow for further processing.
- 3) The convex regions are expanded by assigning labels to non-labeled triangle faces corresponding to the convex regions in the extended BBP. Again for each label only the region with largest connecting area is retained.
- 4) The original results from the random walk algorithm are reevaluated. The random walker algorithm is deemed to have overestimated the diaphragmatic surface region if the number of diaphragmatic labels is more than 25% larger in the diaphragmatic surface region than in the extended BBP or if more than 40% of the labels in the diaphragmatic surface region are non-diaphragmatic labels in the extended BBP. If the diaphragmatic surface region is overestimated the non-diaphragmatic BBP labels in the diaphragmatic surface region are assigned a temporary undefined label to allow for further processing.
- 5) All regions are propagated across currently unassigned feature labels based on the most prevalent label in the minimal BBP of adjacent triangle faces. An example of the propagation algorithm is shown in Figure 9. Regions are only propagated if the newly assigned label does not neighbor existing opposing labels (e.g. anterior labels cannot be assigned adjacent to posterior labels).
- 6) All remaining unassigned triangle faces are assigned a label based on the most prevalent label of their adjacent triangle faces.
- 7) All triangle faces previously assigned with a temporary undefined label are either reassigned by any of the optional repair algorithms (see section 1.2.2.3) or an attempt is made to assign them to the anterior surface region based on the label of adjacent triangle faces and their corresponding label in the minimal BBP. Any triangle faces with undefined labels still remaining after the aforementioned modification are assigned a medial surface region label.
- 8) Any major irregularities in the feature label composition are corrected. Thin one face wide structures are removed and any isolated labels are adjusted and reassigned.
- 9) Lastly, the border connecting adjacent regions is smoothed by readjusting bordering labels to allow for a more gradual and seamless transition between label regions.

## 1.2 Methods

The end result is the set of feature labels  $L$ , depicted in Figure 10, in which six distinct sections of the lung surface are identified; the lateral, medial, anterior, posterior, inferior (or diaphragmatic) and superior surface regions.

### 1.2.2.3 Triangle face label repair

The feature labels of a mesh structure should always be visually inspected after completion of the algorithm. In some edge cases it is possible that the random walker algorithm has incorrectly assigned the feature labels due to the inter-subject variability in the shape of the lungs. When this happens the algorithm cannot properly identify the concave regions in the lung surface. As a result this may cause inaccuracies in the feature labeling of these regions, particularly in the medial surface region. The most common inaccuracies can be corrected for by applying optional repair algorithms. The repair algorithms are all based around an incorrect estimation (either an under- or overestimation) of the medial lung surface during the random walker algorithm. As optional algorithms are applied mid-way during the costal surface subdivision algorithm the entire feature labeling process has to be reapplied by selecting the proper repair algorithm after visual inspection.

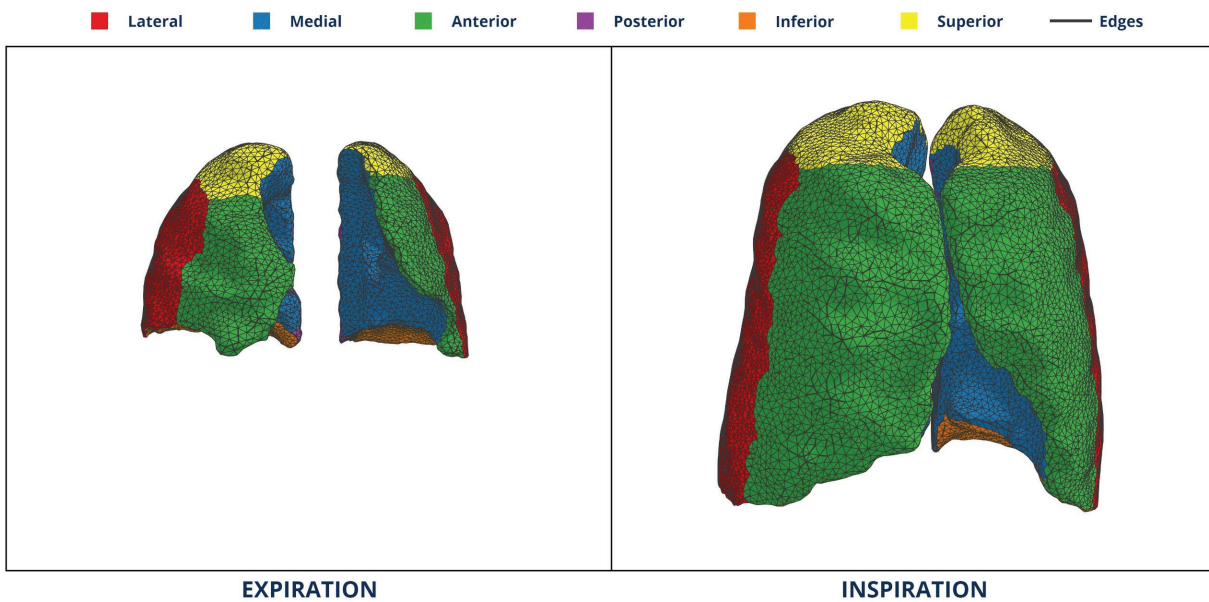


**Figure 10.** An example of the final regions as identified on the surface of the mesh model of the lungs in 3D for the maximal expiration condition (left) and the maximal inspiration condition (right). Both mesh structures are depicted in the same orientation and scale.

There are four different optional repair algorithms, all of which can be selected when initiating the feature labeling. Multiple repair algorithms can be activated at once, if necessary. The first three repair algorithms involve an overestimation of the medial surface region. These algorithms are applied during step 7 of the feature labeling algorithm (see section 1.2.2). The three algorithms are used to reassign the temporary undefined labels to inferior, anterior or posterior labels respectively based on the minimal BBP (and extended BBP for the posterior labels). The final repair algorithm involves an underestimation of the medial surface region. This causes convex region labels to be assigned to triangle faces that should be part of the inner lung. The repair algorithm attempts to restore this region by removing convex label groups larger than 50 triangle faces from this region and reassigning medial labels to these triangle faces based on the extended BBP. An example of the application of a repair algorithm is shown in Figure 11.

## 1.2 Methods

---

Due to the inherent random nature of the random walker algorithm, restarting the feature label algorithm (or even the entire mesh generation algorithm) often provides a slightly different mesh structure with different node positions, face triangles and feature labels. In some cases it might render the use of the optional repair algorithms essentially unnecessary. Therefore if the optional repair algorithms do not provide the expected results, it is recommended that the entire pipeline is simply restarted.

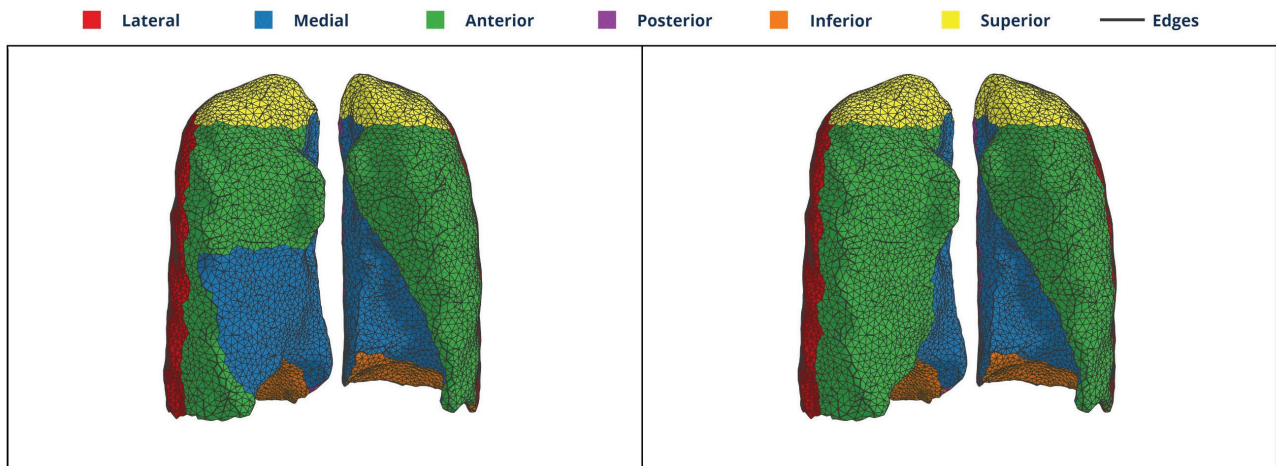


**Figure 11.** An example of the results of an implemented repair algorithm. In the original mesh structure (left) the anterior region of the lung surface is not identified correctly likely due to a lack of a sharp difference in curvature between the medial and anterior region. This leads to a severe overestimation of the medial region. After applying the anterior repair algorithm the mesh structure (right) displays a more appropriate distribution of the regions.

### 1.2.3 Defining lung volume outcomes

The lung volumes are retrieved from the mesh model following the method for feature extraction described by Zhang & Chen (2001). With this method the nodes of every triangle face in the mesh model are connected to origin  $\mathbf{O}$ , an arbitrary position in 3D space, in order to obtain a set of tetrahedrons  $\mathbf{T}$  (see Figure 12). For this model origin  $\mathbf{O}$  is conveniently chosen to be the center of mass of the mesh model. The magnitude of the volume is calculated for every tetrahedron constructed in this manner. The sign of the volume is dependent on the direction of the normal vector of the original triangle face surface. The volume is deemed to be positive if the normal vector is pointing away from the origin  $\mathbf{O}$ , otherwise it is deemed to be negative. The total volume contained within the lung mesh model is determined by summing the volumes of all tetrahedrons in the set of tetrahedrons  $\mathbf{T}$ .

From the mesh model we can derive the total lung capacity ( $TLC_{\text{mesh}}$ ) as the lung volume at maximal inspiration during the breath-hold maneuver and the residual volume ( $RV_{\text{mesh}}$ ) as the lung volume at maximal expiration during the breath-hold maneuver. The VC of the mesh model ( $VC_{\text{mesh}}$ ) is calculated as the change in lung volume of the mesh during an inspiratory maneuver by subtracting  $RV_{\text{mesh}}$  from  $TLC_{\text{mesh}}$ . Additionally the VC is also obtained directly from the spirometry measurements made during the MRI acquisition ( $VC_{\text{spiro}}$ ) in order to compare the VC outcomes between both measurement methods.

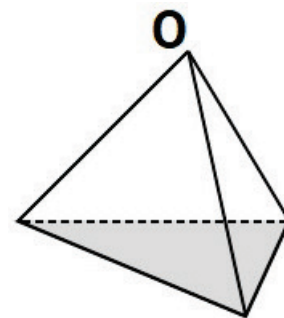


**Figure 12.** A tetrahedron is created for each triangle face (in grey) by connecting the corners to origin  $\mathbf{O}$ .

### 1.2.4 Statistical analysis

All generated mesh structures were visually assessed for inconsistencies and repair algorithms were applied where necessary. The validity of the mesh model was determined by analyzing the difference in lung volumes between the spirometry measurements and volumes derived from the mesh model using Wilcoxon signed rank tests. The strength of the relationship between  $VC_{\text{mesh}}$  and  $VC_{\text{spiro}}$  was evaluated using Spearman's correlation coefficient. The difference in lung volumes between the two measurement methods was further analyzed using Bland-Altman plots. For both the spirometry measurements and the lung volumes derived from the mesh model the overall differences in  $TLC_{\text{mesh}}$ ,  $RV_{\text{mesh}}$ ,  $VC_{\text{mesh}}$  and  $VC_{\text{spiro}}$  between the population groups were assessed with a Kruskal-Wallis test (KWT). Individual differences between the control and two patient subgroups were analyzed with the post-hoc Dunn test. The Bonferroni correction was applied to all probability values if required in order to restrict the effect of multiple testing on differences between the population groups.

## 1.3 Results

The participant characteristics and spirometry results are shown for each subgroup in Table 1.

**Table 1.** Participant characteristics and spirometry results.

	HC (n = 18)	PN (n=13)	PD (n = 22)	<i>p</i> value
Sex (male/female)	8/10	7/6	11/11	0.869
Age (years)	43 ± 14	31 ± 14	45 ± 16	0.030
Length (cm)	178 ± 12	174 ± 9	178 ± 11	0.761
Weight (kg)	79 ± 14	70 ± 13	77 ± 14	0.291
VC <sub>mesh</sub> (L)	4.77 ± 1.35	4.12 ± 0.88	2.76 ± 0.92	<0.001
FVC <sub>supine</sub> (L)	4.92 ± 1.32	4.43 ± 0.95	2.87 ± 1.00	<0.001
FVC <sub>supine</sub> (% predicted)	102 ± 8	94 ± 9	60 ± 12	<0.001
FVC <sub>upright</sub> (L)	5.12 ± 1.38	4.61 ± 0.98	3.84 ± 0.98	0.003
FVC <sub>upright</sub> (% predicted)	106 ± 8	98 ± 9	81 ± 11	<0.001
ΔFVC (L)	0.20 ± 0.18	0.17 ± 0.18	0.94 ± 45	<0.001
ΔFVC (% predicted)	4 ± 4	4 ± 4	22 ± 9	<0.001
MIP (cm H <sub>2</sub> O)	92 ± 23	84 ± 29	61 ± 18	0.002
MIP (% predicted)	106 ± 25	88 ± 28	70 ± 21	0.001
MEP (cm H <sub>2</sub> O)	128 ± 30	106 ± 51	93 ± 27	0.007
MEP (% predicted)	112 ± 28	81 ± 28	80 ± 28	0.002
MEP/MIP ratio	1.4 ± 0.3	1.3 ± 0.4	1.6 ± 0.5	0.079
%MEP/%MIP ratio	1.1 ± 0.3	1.0 ± 0.3	1.2 ± 0.4	0.012

Results are presented for healthy controls (HC), Pompe patients with normal spirometry results (PN) and Pompe patients with decreased spirometry results (PD). Results are reported as mean ± standard deviation except for gender which is reported as the number of males and females. The *p*-values demonstrate the overall differences across population groups as measured using Kruskal Wallis tests and the Chi-square test.

MIP: Maximal Inspiratory Pressure; MEP: Maximal Expiratory Pressure; ΔFVC = FVC<sub>upright</sub> - FVC<sub>supine</sub>

### 1.3.1 Spirometry vital capacity measurements

The VC<sub>spiro</sub> measurements are shown for all participants in Figure 13 and Figure 14a. A KWT indicated that the VC<sub>spiro</sub> measurements were significantly affected by the population groups, *p* < 0.001. Post-hoc Dunn tests revealed that median VC<sub>spiro</sub> measurements were significantly lower in Pompe patients with decreased spirometry results than in healthy controls (*p* < 0.001) as well as in Pompe patients with normal spirometry results (*p* = 0.002). No significant difference in median VC<sub>spiro</sub> measurements was detected between healthy controls and Pompe patients with normal spirometry results (*p* = 1.000).

### 1.3.2 Mesh model lung volume related outcomes

The lung volume measurements retrieved from the mesh model are shown in Figure 13. The VC<sub>mesh</sub> measurements are also shown in Figure 14a. A KWT indicated that the VC measurements derived from the mesh model (VC<sub>mesh</sub>) were significantly affected by the population groups, *p* < 0.001. Additional post-hoc Dunn tests revealed that median VC<sub>mesh</sub> measurements were significantly lower in Pompe patients with decreased spirometry results than in healthy controls (*p* < 0.001) as well as in Pompe patients with normal spirometry results (*p* = 0.001). No significant difference in median VC<sub>mesh</sub> measurements was detected between healthy controls and Pompe patients with normal spirometry results (*p* = 1.000).

### 1.3 Results

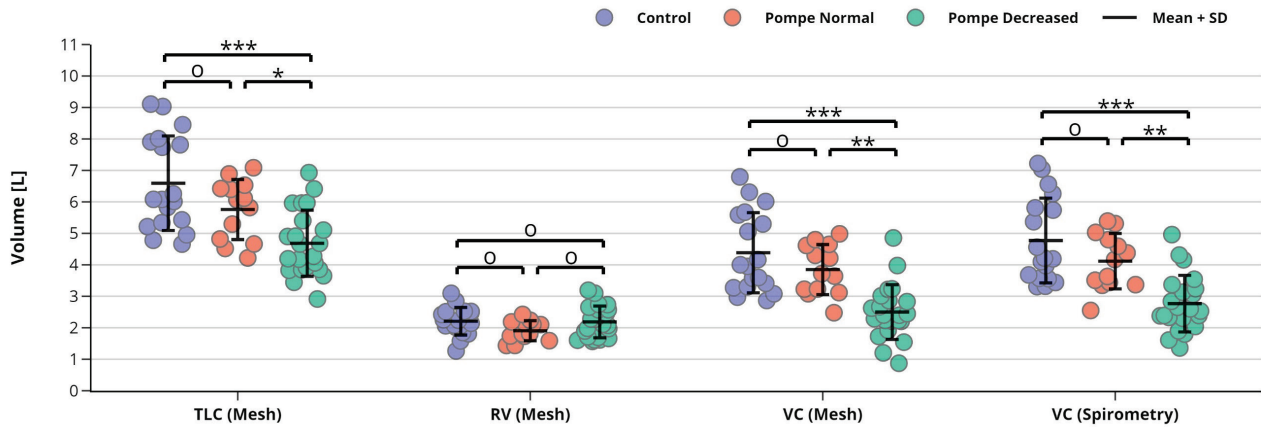


**Figure 13.** A comparison of lung volumes and capacities between population groups. From left to right the total lung capacity (TLC), residual volume (RV) and vital capacity (VC). The VC is depicted both as derived from the mesh and as obtained using the spirometry test. The data for each individual participant is shown as a filled circle with the mean  $\pm$  standard deviation in the centers of the data. The horizontal spread within populations groups is purely for visualization.

O : ns, \* :  $p < 0.05$ , \*\* :  $p < 0.01$ , \*\*\* :  $p < 0.001$ . Control: Healthy controls, Pompe Normal: Pompe patients with normal spirometry results, Pompe Decreased: Pompe patients with decreased spirometry results.

Further analysis on the underlying measurements used to calculate  $VC_{\text{mesh}}$  using another set of Kruskal-Wallis tests indicated that there was no significant difference between population groups for the  $RV_{\text{mesh}}$  measurements retrieved from the mesh model ( $p = 0.168$ ). A significant difference between population groups was however detected for the  $TLC_{\text{mesh}}$  measurements ( $p < 0.001$ ). Post-hoc Dunn tests revealed that median  $TLC_{\text{mesh}}$  measurements were significantly lower in Pompe patients with decreased spirometry results than in healthy controls ( $p < 0.001$ ) as well as in Pompe patients with normal spirometry results ( $p = 0.029$ ). No significant difference in mean  $TLC_{\text{mesh}}$  was detected between the healthy control group and group with Pompe patients with normal spirometry results ( $p = 0.922$ ).

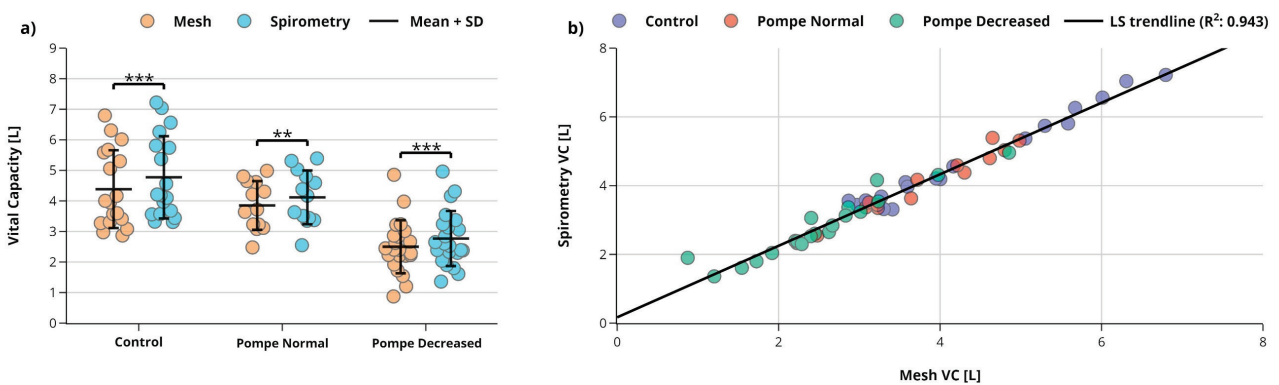


**Figure 14.** A comparison of vital capacity (VC) measurements. The data for each individual participant is shown as a filled circle with the mean  $\pm$  standard deviation in the centers of the data. The horizontal spread within populations groups is purely for visualization. A) The VC as retrieved from the mesh is compared against the VC obtained using spirometry for each population group. B) The VC measurements are plotted against each other for each participant. A least-squares (LS) trendline is plotted across the data ( $R^2 = 0.943$ ).

O : ns, \* :  $p < 0.05$ , \*\* :  $p < 0.01$ , \*\*\* :  $p < 0.001$ . Control: Healthy controls, Pompe Normal: Pompe patients with normal spirometry results, Pompe Decreased: Pompe patients with decreased spirometry results.

### 1.3.3 Level of agreement in determination of vital capacity

A strong significant correlation between the  $VC_{\text{spiro}}$  and  $VC_{\text{mesh}}$  measurements was found,  $r_s = 0.971$ ,  $p < 0.001$ . The correlation plot is shown in Figure 14b. A Wilcoxon signed rank test indicated that across all population groups the median VC was significantly higher when measured using spirometry (3.54 L) than when derived from the mesh model (3.23 L),  $p < 0.001$ . The average bias across all participants was  $0.31 \pm 0.07$  L. Analysis of the level of agreement between the  $VC_{\text{spiro}}$  and  $VC_{\text{mesh}}$  measurements using a Bland-Altman plot shows a consistent pattern of systematic bias (Figure 15a). For almost all participants the VC was higher when measured using spirometry than when retrieved from the mesh model. As depicted in Figure 14a post-hoc Wilcoxon signed rank tests with Bonferroni correction revealed that median  $VC_{\text{spiro}}$  measurements were significantly higher than the median  $VC_{\text{mesh}}$  measurements for healthy controls (bias of  $0.38 \pm 0.11$  L,  $p < 0.001$ ), Pompe patients with normal spirometry results (bias of  $0.27 \pm 0.12$  L,  $p = 0.006$ ) and Pompe patients with decreased spirometry results (bias of  $0.27 \pm 0.12$  L,  $p < 0.001$ ).

Fitting a least squares regression line shows that there appears to be an ascending proportional bias when comparing the two methods ( $R^2 = 0.092$ ). The level of bias is lower in participants with lower mean VC measurements than in participants with higher mean VC measurements. When assessing the differences in VC between both measurement methods as a fraction of the mean VC the systematic bias depicts a more consistent pattern (Figure 15b). On average, the level of systematic bias between both methods is  $9.3 \pm 2.9$  % of the mean VC. This finding was consistent across all population groups as the mean level of systematic bias was found to be  $8.7 \pm 2.8$  % for the healthy controls,  $6.5 \pm 2.7$  % for the Pompe patients with normal spirometry results and  $11.3 \pm 6.8$  % for the Pompe patients with decreased spirometry results.

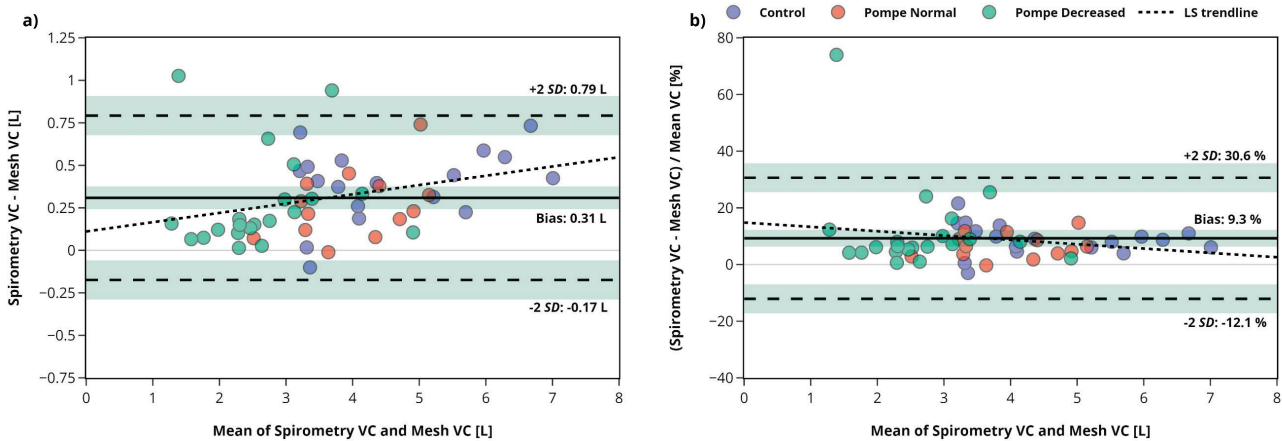


**Figure 15.** Assessment of level of agreement using Bland-Altman plots. The mean level of bias is depicted as a solid black line with the standard error. The limits of agreement are determined as 2x the standard deviation and is depicted as a dashed black line with the standard error. A least-squares (LS) trendline is fitted to the data. A) The difference between the vital capacity (VC) as retrieved from the mesh and as obtained using spirometry is plotted against the mean VC for each participant as a filled circle. B) The relative difference between the two VC measurements (divided by the mean VC) is plotted against the mean VC for each participant as a filled circle.

Control: Healthy controls, Pompe Normal: Pompe patients with normal spirometry results, Pompe Decreased: Pompe patients with decreased spirometry results.

### 1.4 Discussion

In this chapter a pipeline was outlined for the creation of an anatomically accurate three-dimensional mesh model of the lungs based on static breath-hold 3D MRI segmentations at maximal inspiration and maximal expiration to aid in assessing diaphragm function in patients with Pompe disease. Based on face validity it was demonstrated that the anatomical lung surfaces could accurately be identified on the mesh surface with use of the optional repair algorithms, even when the surface of the lungs was shaped highly irregularly. The lung volumes contained within the mesh model of the lungs were validated by comparing VC measurements retrieved from the mesh model against VC measurements obtained using spirometry during the acquisition of the 3D MRI scans.

#### Comparison of VC measurements

Assessment of the lung volumes retrieved from the model indicated that the VC was significantly underestimated, by an average of 0.31 L, for nearly all participants when compared to the VC measurements obtained using spirometry. This offset between measurement methods appears to be dependent on the magnitude of the VC. Analysis of the Bland-Altman plot indicated that the offset in VC measurements was in the region of 10% of the mean VC. Therefore although the difference in VC measurements was significant, it is important to note that the difference was relatively small and consistent for all participants and across population groups. The difference between groups was even larger when comparing the  $VC_{\text{mesh}}$  against the supine FVC measurements made prior to the MRI acquisition (Appendix A). This indicates that the difference in VC measurements is systematic and should therefore not pose an issue when the volumes retrieved from the mesh model are used for comparisons across population groups, nor when then the volumes are used to assess relative contributions to changes in volume during inspiration.

#### Interpreting the difference in VC measurements

In order to provide possible explanations for the underestimation of the VC retrieved from the mesh model of the lungs, two factors can be identified that may be the underlying elements that cause the underestimation. The first factor is an underestimation of the total lung capacity, whilst the other factor is an overestimation of the residual volume. Both factors, individually or combined, can directly contribute to a underestimation of the VC in the mesh model.

Results from previous studies utilizing CT show that the TLC is typically substantially lower in imaging methods than other lung-volume assessment methods such as (body) plethysmography or He-dilution (Bakker et al., 2022; Maurer et al., 2011). However, no further explanation is provided for the difference in TLC between the CT and other lung-volume assessment methods. In these studies the difference in measurement methods was larger (upwards of 0.5 L) than in the current study. A possible explanation for the vastly larger differences found in these studies is the different position in which these measurements were made. In the current study both the MRI acquisition and VC measurements were performed in the supine position, whilst for the other studies the CT scan was performed in the supine position while the VC measurements were obtained in an upright position. It is well documented that there is a significant difference in VC when measured in a supine or upright position (Fromageot et al. 2001), which may therefore explain the larger differences found in the aforementioned studies than in the current study.

## 1.4 Discussion

---

One key factor that may contribute to the underestimation of the TLC using imaging methods is the omission of the anatomical dead space. The anatomical dead space in the respiratory tract is the total volume of air contained within the conducting airways (Quinn et al., 2017). This space spans the entirety of the upper airways and extends all the way down to the level of the terminal bronchioles in the lower airways. No gas exchange takes place in the anatomical dead space. During quiet breathing the anatomical dead space holds about a third of the tidal volume which means it contains, assuming an average tidal volume of 500 ml, about 150 ml of air. During the respiratory cycle the exact volume contained within the anatomical dead space differs slightly. The bronchial diameter increases during inspiration, hereby increasing the volume of air contained within the anatomical dead space. Conversely, the anatomical dead space decreases during expiration as the bronchi and bronchioles contract. The anatomical dead space is not included in the aforementioned CT studies (Bakker et al., 2022; Maurer et al., 2011) nor is it incorporated in the current mesh model, as it only contains the lungs. The current mesh model of the lungs therefore cannot account for the volume changes in the anatomical dead space during the respiratory cycle. By including the anatomical dead space in their analysis of CT data Tantucci et al. (2016) were able to obtain lung volumes that corresponded well with measurements obtained using body plethysmography. They were able to reduce the mean difference in TLC measurements between CT and body plethysmograph to  $0.10 \pm 0.38$  L across all participants for an average TCL of  $7.68 \pm 0.40$  L.

As the current study did not include any TLC measurements using body plethysmography the findings from Tantucci et al. (2016) cannot be directly linked to the current study. Incorporating the anatomical dead space into the mesh model would likely increase the correlation between the VC retrieved from the model and spirometry measurements. However, as previously stated, the relatively minor offset in lung volumes between the measurement methods is inconsequential when comparing the lung volumes derived from the mesh model. Therefore although the inclusion of TLC and RV measurements may provide intriguing information regarding the offset between measurement methods, it is not necessary to include these measurements in a future study in order to utilize the current mesh model.

Lastly it is important to note that most studies assessing spirometry VC measurements have collected their data during an expiratory maneuver. In the current study an inspiratory maneuver was used during the MRI acquisition and spirometry test instead. A recent study indicates that VC measurements may be different when performed in an inspiratory maneuver than in an expiratory maneuver (Barros et al., 2021). It might therefore conceivably be possible that the level of bias between  $VC_{\text{mesh}}$  and  $VC_{\text{spiro}}$  is different depending on the maneuver performed during the spirometry test. In a future study the MRI acquisition and spirometry measurements could be performed during both an inspiratory and expiratory maneuver in order to assess whether the level of bias is different for inspiratory and expiratory VC measurements.

### 1.5 Conclusion

In this chapter we have made use of static breath-hold 3D MRI segmentations of the lungs at maximal inspiration and maximal expiration to generate a three-dimensional mesh model of the lungs in which the anatomical lung surfaces have been identified. Although the VC as retrieved from the mesh model was slightly lower when compared to the VC as measured using spirometry, there was also a high level of correlation in the VC measurements between the two measurement methods. Furthermore the relative difference in VC between measurements retrieved from the mesh model and those obtained using spirometry appeared to be consistent across participants and population groups. The omission of the anatomical dead space in the mesh model of the lungs may provide a possible explanation for the offset in VC measurements between the mesh model and spirometry, as volume changes in the anatomical dead space during inspiration are inherently included in a spirometry VC measurement. Most importantly, the current findings demonstrate that the proposed mesh model can be used as a viable alternative of the conventional spirometry test when assessing the vital capacity of the lungs.

# Chapter 2: Assessing diaphragm function in patients with Pompe disease using 3D mesh model of the lungs

## 2.1 Introduction

In the previous chapter a pipeline was outlined for the creation of a three-dimensional mesh model of the lungs derived from 3D MRI segmentations of the lungs. Previous research into the function of the diaphragm in patients with Pompe disease using imaging methods has mainly been performed using 2D imaging. In these studies the function of the diaphragm is assessed by the motion and shape of the diaphragm in a single plane. The main advantage of the 3D mesh model of the lungs is that it can be used to measure lung volumes directly. In contrast to 2D imaging methods, which are used to estimate lung volumes based on data obtained from a single planar intersection. In the 3D mesh model of the lungs various key topographical segments of the lungs, including the diaphragmatic surface, are identified based on the anatomical surfaces of the lung meshes. The mesh model can thus be used to examine changes in lung volumes during inspiration related to these segments.

The mesh model was proposed as an alternative method for the assessment of respiratory function to conventional PFT measurements, as the mesh model would allow for the assessment of the function of the diaphragm in patients with Pompe disease. In patients with Pompe disease, diaphragm weakness is thought to be one of the first signs indicative of a deterioration in respiratory function (Mellies et al., 2001; van der Beek et al., 2011). Diaphragm weakness can however be difficult to detect due to compensatory efforts of other respiratory muscles. This calls for a sensitive method to assess the diaphragm function of Pompe patients in order to timely start appropriate treatment. Therefore, the main objective of this chapter is to investigate whether diaphragm function and/or impairment can be assessed in patients with Pompe disease using the 3D mesh model of the lungs by examining changes in diaphragm volume during inspiration as well as the contribution of the diaphragm to the total change in lung volume during inspiration.

## 2.2 Methods

### Data acquisition and study population

The dataset used in this chapter was obtained from measurements made in a previous study (Harlaar et al., 2021) and is the same dataset as used in Chapter 1. The dataset contains static breath-hold 3D MRI scans for both maximal inspiration and maximal expiration conditions in 53 participants. Of the 53 participants, 35 were patients with Pompe disease and 18 were healthy age and sex matched controls. Segmentations of each lung in the dataset had been generated from the MRI scans using a deep-learning based algorithm and were processed by experienced analysts. An example of a segmentation is shown in Figure 5. Spirometry data was collected prior to the MRI acquisition in both an upright and supine position ( $FVC_{\text{upright}}$  &  $FVC_{\text{supine}}$ ) as well as during the MRI acquisition in the supine position while performing the breath-hold maneuver ( $VC_{\text{spiro}}$ ). In addition to the FVC measurements, the maximal inspiratory pressure (MIP) and maximal expiratory pressure (MEP) were collected prior to the MRI acquisition. The FVC measurements were also used to calculate  $\Delta FVC$ , the postural drop in FVC. The postural drop in FVC is generally calculated by subtracting the fraction of predicted  $FVC_{\text{supine}}$  values from the fraction of predicted  $FVC_{\text{upright}}$  values. Multiple studies have indicated that the postural drop is a good indicator of diaphragm impairment (Fromageot et al., 2001) even in patients with Pompe disease (Crescimanno et al., 2021; Wens et al., 2015).

Like in the original study from Harlaar et al. (2021) the patients with Pompe disease were subdivided into two subgroups based on their  $FVC_{\text{supine}}$  measurements. In one group patients ( $N = 13$ ) presented with normal spirometry results ( $FVC_{\text{supine}}$  was  $\geq 80\%$  of the predicted value and had a z-score  $\geq -1.64$ ), while the patients in the other group ( $N = 22$ ) presented with decreased spirometry results ( $FVC_{\text{supine}}$  was  $< 80\%$  of the predicted value or had a z-score  $< -1.64$ ).

### Data processing

The mesh generation and feature labeling was performed on both segmented lungs for each participant in Python (Python release 3.9) using the IDE PyCharm Community Edition (version 2022.1). The MRI data was loaded in to Python using the Nibabel library (version 4.0.1). The statistical analysis was performed in both Python and SPSS (version 28). The data was visualized using the interactive graphing library Plotly (version 5.15.0). See Chapter 1 for further details.

### 2.2.1 Adjusting lung segmental allocations based on muscle functions

The volumes related to the topographical segments identified in the three-dimensional mesh model (i.e. the **segmental volumes**) are calculated using the principle described in Chapter 1.3, which was based on the previous work of Zhang & Chen (2001). For each triangle face in the mesh a tetrahedron is created by linking all nodes in the triangle face to origin **O** after which the volume of the tetrahedron can be calculated. In this section the origin **O** is always chosen as the center of mass of the mesh model in the expiration condition. The segmental volumes can then readily be calculated for the expiration condition by summing the volumes of all tetrahedrons in the set of tetrahedrons **T** for which the original surface labels are identical, separately for both sides of the lungs. For the inspiration condition the exact same point in 3D space is chosen as origin **O** (the center of mass in the expiration condition) in order to be able to directly compare the difference in segmental volumes between the expiration and inspiration conditions. The segmental volumes can be calculated by summing volumes of all tetrahedrons that belong to the respective segments. An example for the calculation of the segmental volume is shown for the inferior region in Figure 16. This allocation of the segments is based on the anatomical topographical position and orientation of the segments on the lung surface as outlined in chapter 1 and therefore provides an **anatomical topographical representation** of the segmental volumes.

It is important to note that the volumes attributed to each segment do not translate directly to the functional contributions of the respiratory muscles in the anatomical topographical representation of the segments. As the segmental volumes are based on the volume associated with the triangle faces on the surface of the mesh, an increase in the surface area of a segment will consequently bring about an increase in volume associated to this segment. In order to establish a more functional topographical representation of the segmental volumes related to the actual functional contribution of the respiratory muscles it is therefore crucial to correctly identify the underlying movements that lead to the increase in surface area of a segment. Figure 17 shows an example of the change in lung surface area for the posterior segment during the inspiratory maneuver that brings about the change in segmental volume. It is evident that the expansion of the posterior segment surface area during inspiration can be attributed to an extension of the posterior segment in the inferior as well as the lateral direction. The increase in surface area of the posterior segment in the inferior direction can only be caused by the contraction of the diaphragm during inspiration. Conversely the increase in the lateral direction is caused by the expansion of the rib cage due to activity of the external intercostal muscles. The segmental volume associated to the region that describes the change in lung surface during inspiration (the ‘reallocated’ region in Figure 17) has to be reallocated accordingly in order to establish a more functional topographical representation of the segmental volumes related to the underlying respiratory muscle functions.

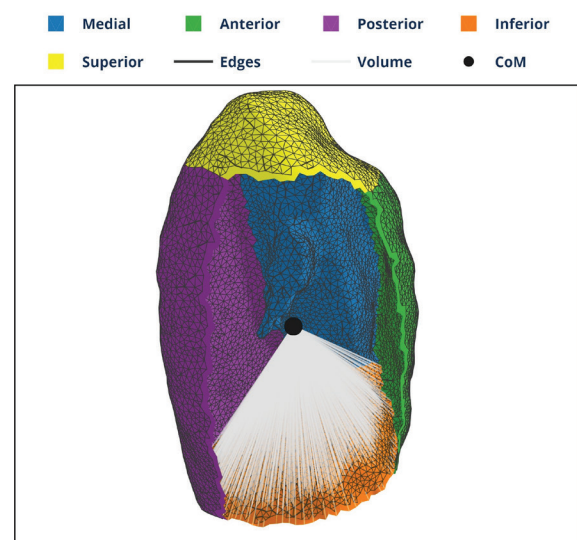


**Figure 16.** A sagittal view of the right lung with the lateral segment cut out showing the calculation of the inferior segmental volume. Tetrahedrons are created by linking all triangle faces to origin **O** in the center of mass (CoM). The inferior segmental volume is the summed volume of all

## 2.2 Methods

The reallocation of segmental volumes is performed for all segments except for the superior segment. The superior segment cannot be affected by activity of the diaphragm. An increase in segmental volume of the superior regions during inspiration is, in the current 3D model, solely deemed to be due to activity of the external intercostal muscles. The intercostal muscles are capable of elevating the rib cage hereby increasing the volume associated with the superior segmental surface region. For all remaining segments the segmental volumes are reallocated to the lateral, anterior and/or inferior segment regions. The segmental volumes were not reallocated to the posterior and medial segment regions as there are no major muscle groups involved during inspiration at the posterior and medial regions of the lungs.

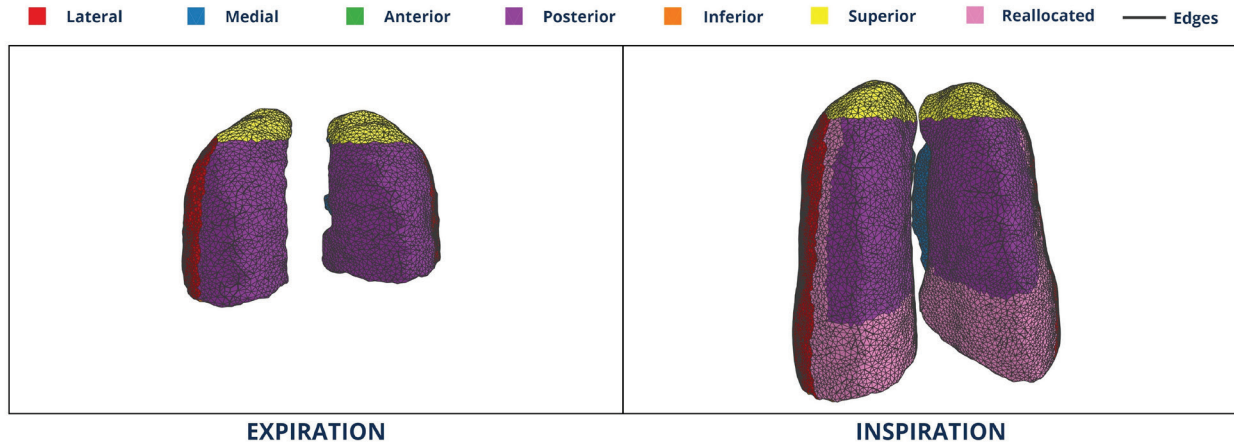


**Figure 17.** An example of the segment reallocation. The pink ‘*Reallocated*’ section visible on the mesh in the maximal inspiration condition (right) signifies the subsection of the surface of the posterior segment that increases during the inspiratory maneuver. The segmental volume associated with this region is reallocated to other based on the change in dimensions of the original posterior segment. Both meshes are depicted in the same orientation and scale.

The regions for which the segmental volumes are to be reallocated are based on the average position of the borders between adjacent segments in the maximal expiration condition. The region is established by applying the determined position of the border to the maximal inspiration condition. The region of the original segment in the inspiration condition that falls outside of these borders is the region that will be reallocated, the **reallocated** region. For the maximal inspiration condition the average position of the border is calculated based on the border between the newly identified reallocated region and the adjacent segments. The difference in average position of these borders between the maximal expiration and maximal inspiration conditions are used to determine the average change in dimensions in the lateral, anterior and inferior direction. The magnitude of the average change in dimensions for each of these directions is used to determine the allocation ratio **AR**, which is calculated using Equation 3.

$$AR_{\text{segment}} = \frac{\Delta\text{dimension}_{\text{segment}}}{(\Delta\text{dimension}_{\text{lateral}} + \Delta\text{dimension}_{\text{anterior}} + \Delta\text{dimension}_{\text{inferior}})} \quad (3)$$

As an example, for the left side of the mesh structure of the lungs as depicted in Figure 17 the average change in lateral direction of the reallocated posterior region is 13.0 mm, while the average change in the inferior direction is 77.4 mm. The posterior region cannot extend in the anterior direction, therefore the average change in the anterior direction is 0 mm. The result of Equation 3 for the lateral segment is  $13.0 / (13.0 + 0 + 77.4) = 0.144$  and the result for the inferior segment is  $77.4 / (13.0 + 0 + 77.4) = 0.856$ . For this reallocated posterior region 14.4 % of the segmental volume will be added to

## 2.2 Methods

---

the lateral segmental volume while the remaining 85.6 % will be added to the inferior segmental volume. This process is repeated for all aforementioned segments on both sides of the lungs. At completion of the algorithm the segmental volumes reflect the underlying respiratory muscle functions more closely. The reallocation of the segmental volumes therefore provides a more **functional topographical representation** of the segmental volumes.

### 2.2.2 Mesh model related outcomes

The segmental volumes described in the previous section are normalized against the baseline RV measurements using Equation 4 for all participants in order to compensate for differences in the participant characteristics between population groups. Results for the segmental volumes are reported as both the normalized and non-normalized segmental volumes. The normalized segmental volumes are used when comparing segmental volumes across population groups unless otherwise specified.

$$\text{Normalized segmental volume} = \left( \frac{\text{Segmental volume}}{\text{Residual volume}} \right) \times 100\% \quad (4)$$

#### 2.2.2.1 Defining the diaphragm and costal segments

The diaphragm segment is deemed to identical to the inferior segment as the inferior segment is based on the anatomical topographical positioning of the diaphragmatic lung surface. In order to assess the relative contributions of the diaphragm and the other inspiratory muscles (predominantly the external intercostal muscles) the contribution of the diaphragm segment is compared against the contribution of the **costal segment**. The costal segment is comprised of the lateral, anterior and superior segments as identified in the mesh model. The (change in) costal segmental volume is therefore the sum of the (change in) segmental volumes of the lateral, anterior and superior segments (Equation 5). In order to compare the diaphragm and costal segment the diaphragm/costal ratio was calculated by dividing the change in diaphragm volume by the change in costal volume.

$$\text{Costal volume} = \text{Lateral volume} + \text{Anterior volume} + \text{Superior volume} \quad (5)$$

In order to assess the volume of the main sections of the lungs that are involved during inspiration the volumes of the diaphragm and costal segments are combined to define the **summed diaphragm and costal (SDC)** volume. As was the case for the segmental volumes, the SDC volumes were also normalized against the baseline RV measurements for all participants in order to compensate for differences in the participant characteristics between population groups.

#### 2.2.2.2 Lung size related outcomes

In studies using 2D imaging the function of the diaphragm is generally assessed by examining outcome measures relating to change in shape of the diaphragm, such as the superoinferior (SI) lung size and ratio (Gaeta et al., 2015; Harlaar et al., 2021; Wens et al., 2015). In this study the SI lung size is determined as the vertical difference between the maximal vertical position of the inferior (or diaphragmatic) segment (the apex of the diaphragm) and the maximal vertical position of the superior segment (the apex of the lungs). Prior to the SI lung size calculation the surface of inferior segment was first eroded by the five outermost layers of triangle faces in order to reduce the effect of possible incorrectly identified triangle face labels at the edge of the inferior segment. Furthermore, some participants with severe progression of Pompe disease showed a highly irregular shape of the diaphragm. Removing the five outermost layers of the inferior segment substantially reduced the probability that the apex of the diaphragm would be incorrectly identified. The SI ratio is calculated by dividing the SI lung size at maximal inspiration by the SI lung size at maximal expiration.

## 2.2 Methods

---

The anteroposterior (AP) lung size is determined as the difference in the anteroposterior axis between the most anterior position of the anterior segment and the most posterior position of the posterior segment. The AP ratio is calculated by dividing the AP lung size at maximal inspiration by the AP lung size at maximal expiration. A rough visualization of the SI and AP sizes is depicted in Figure 4.

### 2.2.3 Statistical analysis

All generated mesh structures were visually assessed for inconsistencies and repair algorithms were applied where necessary. Overall differences in expiratory and inspiratory segmental volumes between the population groups were assessed with a Kruskal-Wallis test (KWT). Overall differences in change in segmental volume during inspiration as well as the relative segmental contributions to the total increase in lung volume during inspiration were also assessed with a KWT. Finally, a KWT was also used to assess for overall differences in SI and AP lung sizes and ratios between population groups. Individual differences between the control and two patient subgroups for all outcomes were analyzed with the post-hoc Dunn test. The Bonferroni correction was applied to all probability values if required in order to restrict the effect of multiple testing on differences between the population groups. Segmental volume results were compared against the SI and AP lung size outcomes as well as the PFT results using Spearman's correlation coefficient.

## 2.3 Results

The participant characteristics and spirometry results are shown for each subgroup in Table 1.

### 2.3.1 Expiratory segmental volumes

Table 2 contains the expiratory segmental volumes alongside the inspiratory segmental volumes in both the anatomical and functional topographical representations. A small but significant difference in normalized expiratory volumes was found between population groups for the lateral ( $p = 0.030$ ) and medial ( $p = 0.030$ ) segments using a KWT. A post-hoc Dunn test showed that the median normalized expiratory volume was significantly lower in Pompe patients with normal spirometry results than in Pompe patients with decreased spirometry results for the lateral segment ( $p = 0.038$ ). For the medial segment the median normalized expiratory volume was significantly higher in Pompe patients with normal spirometry results than in Pompe patients with decreased spirometry results ( $p = 0.041$ ). No other significant effects were found between population groups,  $p > 0.050$ . The normalized expiratory segmental volumes are shown in Figure 18a.

**Table 2.** Expiratory and inspiratory segmental volumes as derived from the mesh.

		Segmental Volume (L)					
		Lateral	Medial	Anterior	Posterior	Inferior	Superior
Expiratory	HC	0.57 ± 0.12	0.02 ± 0.03	0.41 ± 0.12	0.71 ± 0.15	0.12 ± 0.04	0.38 ± 0.09
	PN	0.46 ± 0.10	0.05 ± 0.03	0.33 ± 0.10	0.61 ± 0.11	0.13 ± 0.05	0.32 ± 0.06
	PD	0.56 ± 0.14	0.02 ± 0.05	0.40 ± 0.13	0.70 ± 0.17	0.13 ± 0.05	0.38 ± 0.10
	$p$ value	0.032	0.053	0.110	0.151	0.508	0.069
Inspiratory (Anatomical)	HC	1.58 ± 0.34	0.30 ± 0.11	1.44 ± 0.40	1.52 ± 0.31	0.89 ± 0.31	0.86 ± 0.16
	PN	1.39 ± 0.26	0.24 ± 0.05	1.32 ± 0.27	1.30 ± 0.20	0.80 ± 0.16	0.72 ± 0.13
	PD	1.16 ± 0.25	0.13 ± 0.10	1.18 ± 0.27	1.06 ± 0.27	0.41 ± 0.29	0.75 ± 0.16
	$p$ value	<0.001	<0.001	0.083	<0.001	<0.001	0.029
Inspiratory (Functional)	HC	0.88 ± 0.21	0.17 ± 0.04	1.56 ± 0.38	0.86 ± 0.17	2.25 ± 0.73	0.86 ± 0.16
	PN	0.67 ± 0.18	0.15 ± 0.04	1.45 ± 0.32	0.75 ± 0.14	2.02 ± 0.40	0.72 ± 0.13
	PD	0.78 ± 0.21	0.12 ± 0.05	1.29 ± 0.27	0.79 ± 0.19	0.97 ± 0.79	0.75 ± 0.16
	$p$ value	0.027	0.003	0.045	0.112	<0.001	0.029

Segmental volumes are presented for healthy controls (HC), Pompe patients with normal spirometry results (PN) and Pompe patients with decreased spirometry results (PD). Volumes are reported as mean ± standard deviation. The  $p$ -values demonstrate the overall differences across population groups as measured using Kruskal Wallis tests. Results are shown for the expiratory segmental volumes as well as the inspiratory segmental volumes for both the anatomical topographical representation and the functional topographical representation.

### 2.3.2 Segmental volumes in the anatomical topographical representation

The normalized inspiratory volumes for all segments in the original anatomical topographical representation are shown in Figure 18b. As indicated by a KWT, the normalized inspiratory volumes were significantly affected by population groups for all segments. Post-hoc Dunn tests revealed that there were no significant differences in median normalized inspiratory segmental volumes between the healthy controls and Pompe patients with normal spirometry results ( $p > 0.050$ ). The median normalized inspiratory volumes were however significantly higher in healthy controls than in Pompe patients with decreased spirometry results for all segments (anterior:  $p = 0.038$ , superior:  $p = 0.046$ , others:  $p < 0.001$ ). Additionally the median normalized inspiratory volumes were also significantly higher in Pompe patients with normal spirometry results than in Pompe patients

## 2.3 Results

with decreased spirometry results for all segments except for the superior segment (superior:  $p > 0.050$ , anterior:  $p = 0.006$ , posterior:  $p = 0.001$ , others:  $p < 0.001$ ).

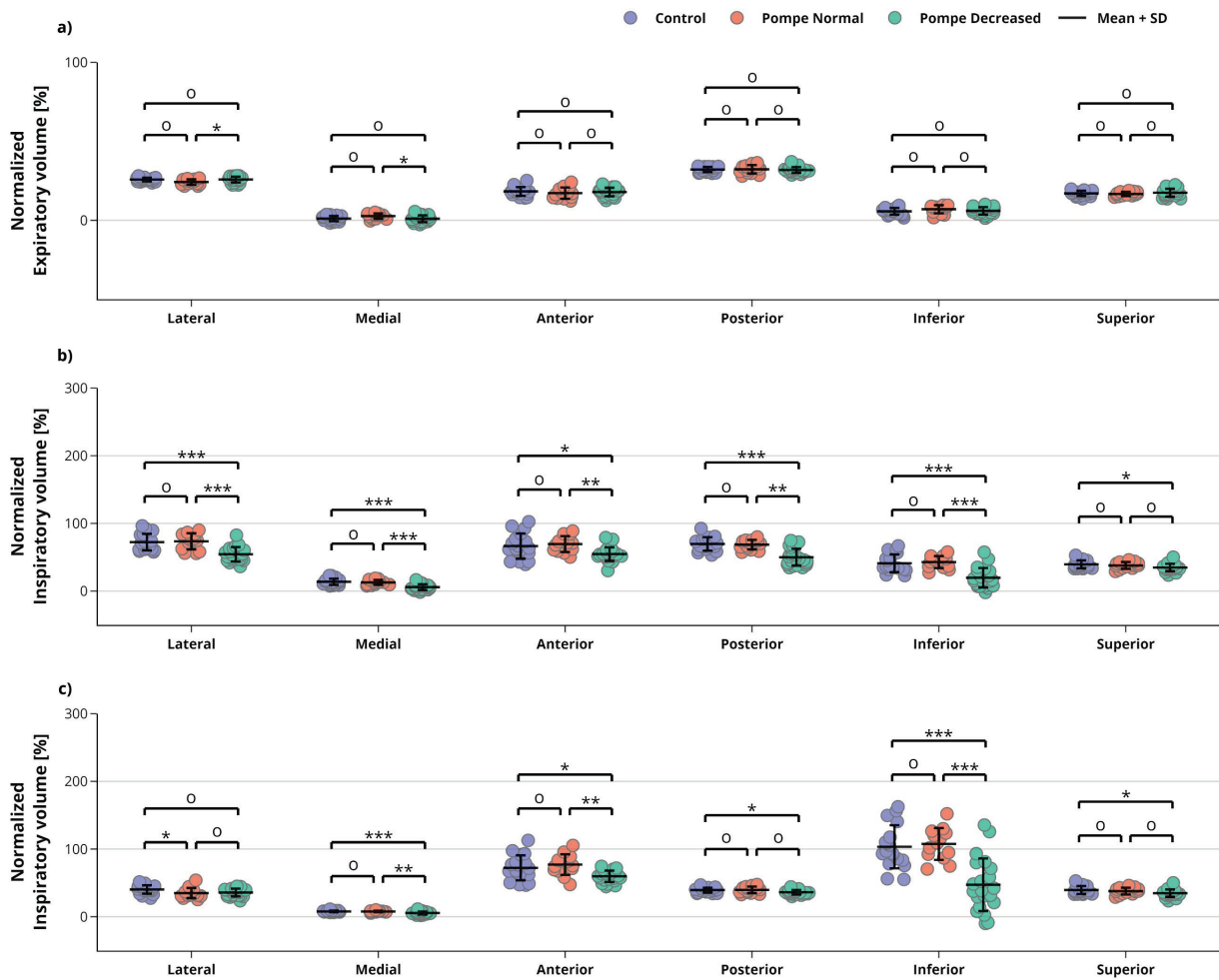


**Figure 18.** The normalized expiratory and inspiratory segmental volumes are depicted for each segment and population group. The data for each individual participant is shown as a filled circle with the mean  $\pm$  standard deviation in the centers of the data. The horizontal spread within populations groups is purely for visualization. The volumes are shown as derived from the mesh in the maximal expiration condition (a) and the maximal inspiration condition in both the anatomical representation (b) and the functional representation (c).

O : ns, \* :  $p < 0.05$ , \*\* :  $p < 0.01$ , \*\*\* :  $p < 0.001$ . Control: Healthy controls, Pompe Normal: Pompe patients with normal spirometry results, Pompe Decreased: Pompe patients with decreased spirometry results.

The changes in normalized segmental volumes during inspiration are depicted for the anatomical topographical representation in Figure 19a. A set of KWTs indicated that the changes in normalized segmental volumes were significantly affected by population groups for all segments. Post-hoc Dunn tests revealed that there were no significant differences in median normalized segmental volumes between the healthy controls and Pompe patients with normal spirometry results ( $p > 0.050$ ). The median change in normalized volumes was significantly higher in healthy controls than in Pompe patients with decreased spirometry results for all segments except for the lateral segment (lateral:  $p > 0.050$ , superior:  $p = 0.035$ , others:  $p < 0.001$ ). Additionally the median change in normalized volumes was also significantly higher in Pompe patients with normal spirometry results than in Pompe patients with decreased spirometry results for all segments except for the superior segment (superior:  $p > 0.050$ , medial:  $p = 0.002$ , anterior:  $p = 0.012$ , posterior:  $p = 0.001$ , others:  $p < 0.001$ ).

## 2.3 Results

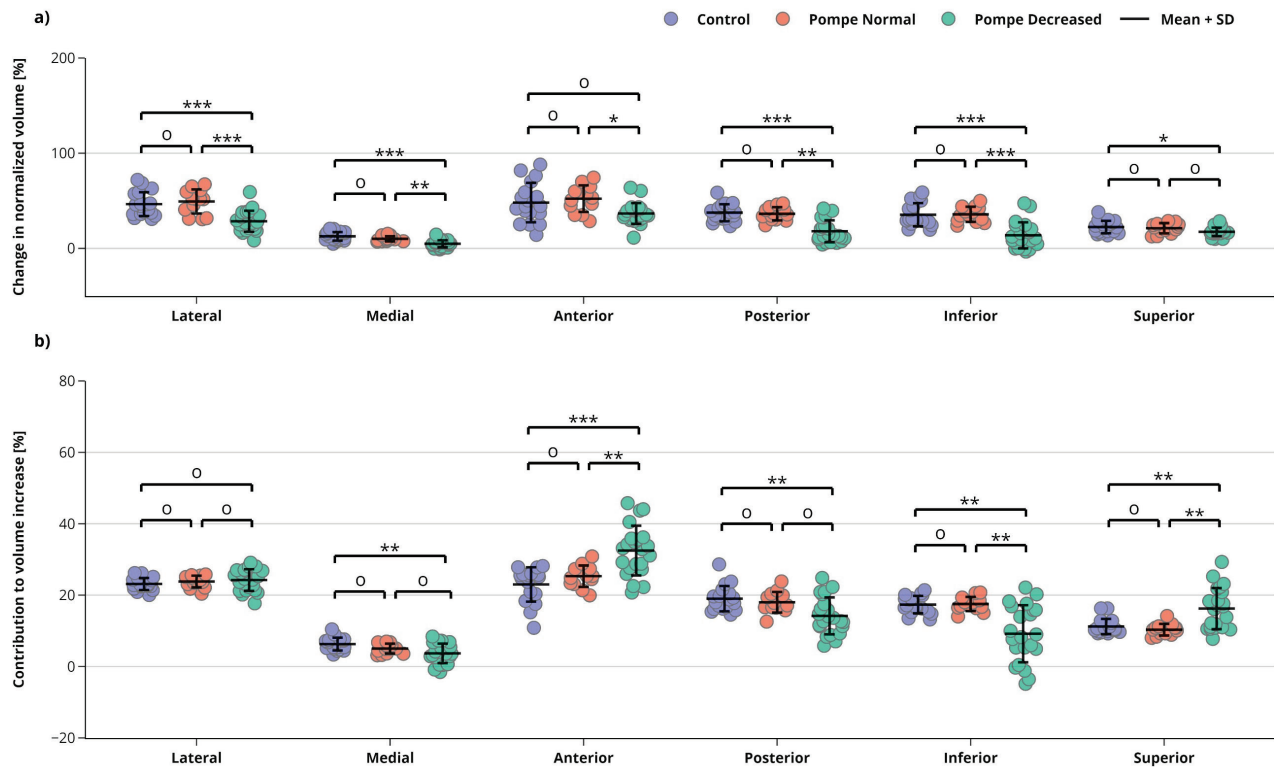


**Figure 19.** The segmental lung volume related measurements obtained from the mesh in the anatomical representation. The data for each individual participant is shown as a filled circle with the mean  $\pm$  standard deviation in the centers of the data. The horizontal spread within populations groups is purely for visualization. A) The change in normalized volume for each segment. B) The relative contribution to the total change in lung volume during inspiration for each segment. O : ns, \* :  $p < 0.05$ , \*\* :  $p < 0.01$ , \*\*\* :  $p < 0.001$ . Control: Healthy controls, Pompe Normal: Pompe patients with normal spirometry results, Pompe Decreased: Pompe patients with decreased spirometry results.

The relative contribution of each segment to the total change in lung volume during inspiration is shown for the anatomical topographical representation in Figure 19b. A set of KWTs indicated that the relative contributions were significantly affected by population groups for all segments except for the lateral segment ( $p > 0.050$ ). Post-hoc Dunn tests revealed that there were no significant differences in median contribution between the healthy controls and Pompe patients with normal spirometry results ( $p > 0.050$ ). The median contributions were significantly higher in healthy controls than in Pompe patients with decreased spirometry results for the medial ( $p = 0.004$ ), posterior ( $p = 0.007$ ) and inferior ( $p = 0.003$ ) segments while they were significantly lower for the anterior ( $p < 0.001$ ), and superior ( $p = 0.005$ ) segments. Additionally the median contributions were also significantly lower in Pompe patients with normal spirometry results than in Pompe patients with decreased spirometry results for the anterior ( $p = 0.006$ ) and superior ( $p = 0.001$ ) segments while the median inferior contributions were significantly higher ( $p = 0.004$ ).

### 2.3.3 Segmental volumes in the functional topographical representation

The normalized inspiratory volumes for all reallocated segments are shown for the functional topographical representation in Figure 18c. As was the case in the anatomical topographical representation, the normalized inspiratory volumes were significantly affected by population groups for all segments when assessed using KWTs. On average the normalized inspiratory volumes were lower in the anatomical topographical representation than in the functional topographical representation for the

## 2.3 Results

lateral, medial and posterior segments across all population groups, while they were higher for the anterior and inferior segments. The normalized inspiratory superior volumes were unchanged for the anatomical and functional topographical representations. For the functional topographical representation post-hoc Dunn tests revealed that the median normalized inspiratory volumes were significantly higher in healthy controls than in Pompe patients with normal spirometry results for all segments except for the lateral segment (lateral:  $p > 0.050$ , anterior:  $p = 0.047$ , posterior:  $p = 0.033$ , superior =  $0.046$ , others:  $p < 0.001$ ). Additionally the median normalized inspiratory volumes were also significantly higher in Pompe patients with normal spirometry results than in Pompe patients with decreased spirometry results for the medial ( $p = 0.002$ ), anterior ( $p = 0.003$ ) and inferior ( $p < 0.001$ ) segments. Lastly, in contrast to the anatomical topographical representation, the median normalized inspiratory volume was also found to be significantly higher for the lateral segment in healthy controls than in Pompe patients with normal spirometry results ( $p = 0.044$ ) for the functional topographical representation.

**Table 3.** Change in segmental volumes during inspiration for the anatomical and functional topographical representations.

	Anatomical topographical representation				Functional topographical representation			
	HC	PN	PD	$p$ value	HC	PN	PD	$p$ value
$\Delta$ Lateral volume (L)	1.01 $\pm$ 0.27	0.92 $\pm$ 0.23	0.60 $\pm$ 0.21	<0.001	0.31 $\pm$ 0.14	0.20 $\pm$ 0.14	0.21 $\pm$ 0.12	0.035
$\Delta$ Medial volume (L)	0.28 $\pm$ 0.12	0.19 $\pm$ 0.04	0.10 $\pm$ 0.08	<0.001	0.15 $\pm$ 0.06	0.10 $\pm$ 0.05	0.10 $\pm$ 0.04	0.006
$\Delta$ Anterior volume (L)	1.03 $\pm$ 0.41	0.99 $\pm$ 0.28	0.78 $\pm$ 0.22	0.064	1.16 $\pm$ 0.39	1.12 $\pm$ 0.34	0.89 $\pm$ 0.20	0.024
$\Delta$ Posterior volume (L)	0.81 $\pm$ 0.20	0.68 $\pm$ 0.13	0.37 $\pm$ 0.21	<0.001	0.15 $\pm$ 0.05	0.14 $\pm$ 0.06	0.09 $\pm$ 0.05	<0.001
$\Delta$ Inferior volume (L)	0.78 $\pm$ 0.29	0.67 $\pm$ 0.13	0.28 $\pm$ 0.28	<0.001	2.12 $\pm$ 0.72	1.88 $\pm$ 0.38	0.84 $\pm$ 0.78	<0.001
$\Delta$ Superior volume (L)	0.48 $\pm$ 0.12	0.40 $\pm$ 0.11	0.37 $\pm$ 0.09	0.006	0.48 $\pm$ 0.12	0.40 $\pm$ 0.11	0.37 $\pm$ 0.09	0.006

The changes in segmental volumes during inspiration are presented for healthy controls (HC), Pompe patients with normal spirometry results (PN) and Pompe patients with decreased spirometry results (PD). Volumes are reported as mean  $\pm$  standard deviation. The  $p$ -values demonstrate the overall differences across population groups as measured using Kruskal Wallis tests.

**Table 4.** Change in diaphragm and costal volumes during inspiration for the anatomical and functional topographical representations.

	Anatomical topographical representation				Functional topographical representation			
	HC	PN	PD	$p$ value	HC	PN	PD	$p$ value
$\Delta$ Diaphragm volume (L)	0.78 $\pm$ 0.29	0.67 $\pm$ 0.13	0.28 $\pm$ 0.28	<0.001	2.12 $\pm$ 0.72	1.88 $\pm$ 0.38	0.84 $\pm$ 0.78	<0.001
$\Delta$ Costal volume (L)	2.52 $\pm$ 0.76	2.31 $\pm$ 0.60	1.75 $\pm$ 0.46	0.002	1.95 $\pm$ 0.55	1.73 $\pm$ 0.48	1.47 $\pm$ 0.33	0.020

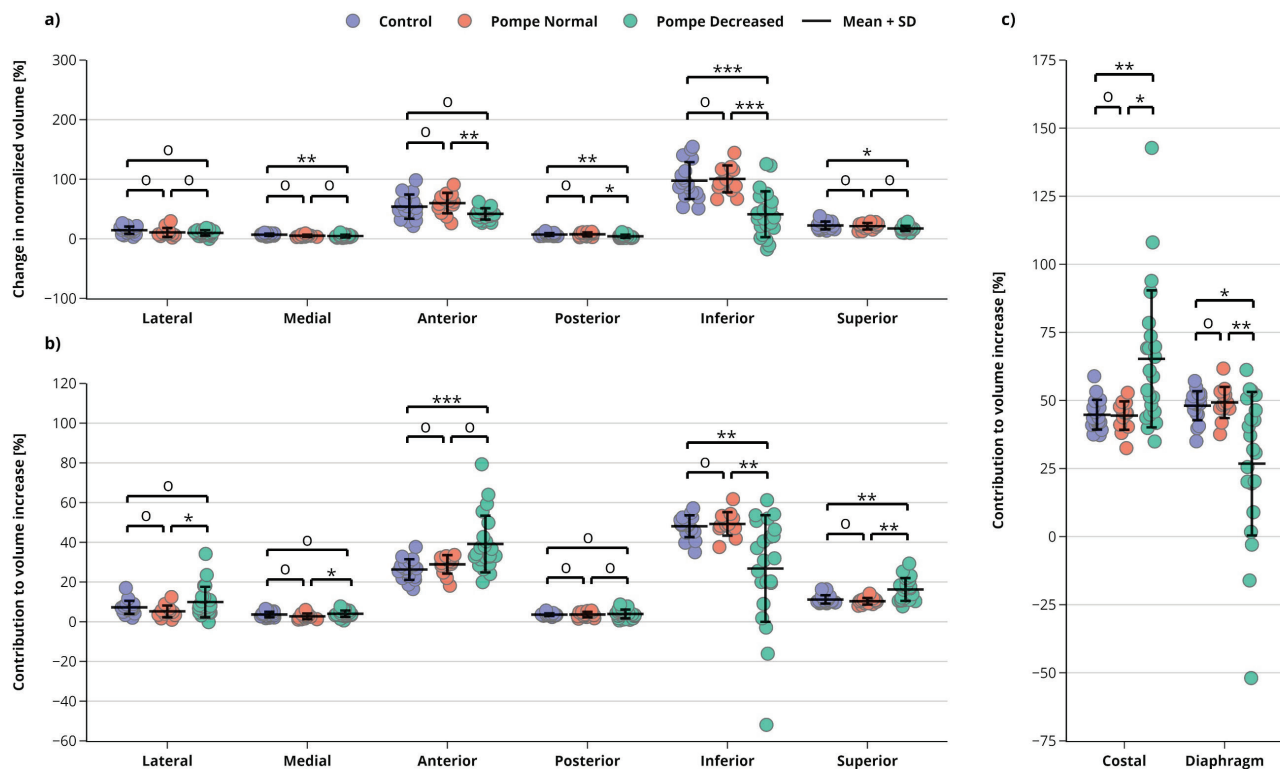
The changes in diaphragm and costal volumes during inspiration are presented for healthy controls (HC), Pompe patients with normal spirometry results (PN) and Pompe patients with decreased spirometry results (PD). Volumes are reported as mean  $\pm$  standard deviation. The  $p$ -values demonstrate the overall differences across population groups as measured using Kruskal Wallis tests.

Table 3 presents the mean change in segmental volumes for each population group in both the anatomical and functional topographical representations. The changes in normalized segmental volumes during inspiration are depicted for the functional topographical representation in Figure 20a. A set of KWTs indicated that the change in normalized segmental volumes for the functional topographical representation was significantly affected by population groups for all segments except for the lateral segment (lateral:  $p > 0.050$ , medial:  $p = 0.004$ , anterior:  $p = 0.006$ , posterior:  $p = 0.002$ , inferior:  $p < 0.001$ , superior:  $p = 0.024$ ). Post-hoc Dunn tests revealed that there were no significant differences in median normalized segmental volumes between the healthy controls and Pompe patients with normal spirometry results ( $p > 0.050$ ). The median change in normalized volumes was significantly higher in healthy controls than in Pompe patients with decreased spirometry results for

## 2.3 Results

the medial ( $p = 0.003$ ), posterior ( $p = 0.008$ ), inferior ( $p < 0.001$ ) and superior ( $p = 0.035$ ) segments. Additionally the median change in normalized volumes was also significantly higher in Pompe patients with normal spirometry results than in Pompe patients with decreased spirometry results for the anterior ( $p = 0.007$ ), posterior ( $p = 0.011$ ) and inferior ( $p < 0.001$ ) segments.

The relative contribution of each segment to the total change in lung volume during inspiration is shown for the functional topographical representation in Figure 20b. On average the relative contributions were substantially lower for the lateral and posterior segments in the anatomical topographical representation than in the functional topographical representation across all population groups, while they were slightly and substantially higher for the anterior and inferior segments respectively. A set of KWTs indicated that the relative contributions were significantly affected by population groups for all segments except for the posterior segment ( $p > 0.050$ ). Post-hoc Dunn tests revealed that there were no significant differences in median contribution between the healthy controls and Pompe patients with normal spirometry results ( $p > 0.050$ ). The median contributions were significantly lower in healthy controls than in Pompe patients with decreased spirometry results for the anterior ( $p < 0.001$ ) and superior ( $p = 0.005$ ) segments while the median inferior contributions were significantly higher ( $p = 0.009$ ). Additionally the median contributions were also significantly lower in Pompe patients with normal spirometry results than in Pompe patients with decreased spirometry results for the lateral ( $p = 0.038$ ), medial ( $p = 0.020$ ) and superior ( $p = 0.001$ ) segments while the median inferior contributions were again significantly higher ( $p = 0.009$ ).



**Figure 20.** The segmental lung volume related measurements obtained from the mesh in the functional representation. The data for each individual participant is shown as a filled circle with the mean  $\pm$  standard deviation in the centers of the data. The horizontal spread within populations groups is purely for visualization. A) The change in normalized volume for each segment. B) The relative contribution to the total change in lung volume during inspiration for each segment. C) A detailed comparison between the relative contributions of the diaphragm and costal segments to the total change in volume during inspiration. O : ns, \* :  $p < 0.05$ , \*\* :  $p < 0.01$ , \*\*\* :  $p < 0.001$ . Control: Healthy controls, Pompe Normal: Pompe patients with normal spirometry results, Pompe Decreased: Pompe patients with decreased spirometry results.

## 2.3 Results

### 2.3.4 Diaphragm and costal segment volume and contribution

The mean change in diaphragm and costal volumes for each population group in both the anatomical and functional topographical representations are presented in Table 4. A significant effect between population groups was found using a KWT for the change in normalized costal volume during inspiration for both the anatomical topographical representation ( $p < 0.001$ ) and the functional topographical representation ( $p = 0.013$ ). Post hoc Dunn tests revealed that the median normalized costal volume was significantly higher in healthy controls than in Pompe patients with normal spirometry results for the anatomical topographical representation ( $p = 0.011$ ) but not in the functional topographical representation ( $p > 0.050$ ). The median normalized costal volume was also significantly higher in Pompe patients with normal spirometry results than in Pompe patients with decreased spirometry results for both the anatomical ( $p = 0.002$ ) and functional ( $p = 0.030$ ) topographical representations. No differences were found between healthy controls and Pompe patients with normal spirometry results ( $p > 0.050$ ).

The relative contributions of the costal segment to the change in volume during inspiration is shown in Figure 20c for the functional topographical representation. A KWT indicated that the costal contribution to the total change in lung volume was significantly affected by population groups ( $p = 0.001$ ). Post hoc Dunn tests revealed that the median costal contribution was lower in healthy controls than in Pompe patients with normal spirometry results ( $p = 0.003$ ). Additionally the median costal contribution was also significantly higher in Pompe patients with normal spirometry results than in Pompe patients with decreased spirometry results ( $p = 0.013$ ). Again no difference was found between healthy controls and Pompe patients with normal spirometry results ( $p = 1.000$ ).

Only three participants presented with a negative diaphragm contribution to the increase in volume during the inspiratory maneuver. Two participants in particular (both Pompe patients with decreased spirometry results) displayed a substantial deviating result with regard to the relative contributions of the diaphragm and costal segments. These participants displayed a comparatively large negative contribution of the diaphragm segment (-51.9 % and -16.1 % respectively) and large contribution of the costal segment (142.7 % and 108.0 % respectively) to the total increase in lung volume during inspiration.

### 2.3.5 Summed diaphragm and costal volumes and ratios

Table 5 presents the mean change in (normalized) summed diaphragm and costal (SDC) segmental volumes and diaphragm/costal ratio for each population group in both the anatomical and functional topographical representations. The diaphragm/costal ratio as well as the SDC and normalized SDC volumes were substantially higher in the functional topographical representation than in the anatomical topographical representation.

**Table 5.** Changes in summed diaphragm and costal volumes and diaphragm/costal ratio.

	Anatomical topographical representation				Functional topographical representation			
	HC	PN	PD	$p$ value	HC	PN	PD	$p$ value
$\Delta$ SDC volume (L)	3.29 $\pm$ 1.02	2.98 $\pm$ 0.70	2.03 $\pm$ 0.66	<0.001	4.08 $\pm$ 1.21	3.61 $\pm$ 0.76	2.31 $\pm$ 0.86	<0.001
$\Delta$ SDC <sub>NORM</sub> volume (%)	152 $\pm$ 49	158 $\pm$ 37	96 $\pm$ 34	<0.001	188 $\pm$ 57	192 $\pm$ 42	110 $\pm$ 45	<0.001
$\Delta$ Diaphragm / $\Delta$ Costal ratio	0.31 $\pm$ 0.06	0.30 $\pm$ 0.05	0.15 $\pm$ 0.14	<0.001	1.10 $\pm$ 0.24	1.14 $\pm$ 0.30	0.59 $\pm$ 0.54	<0.001

Results are presented for healthy controls (HC), Pompe patients with normal spirometry results (PN) and Pompe patients with decreased spirometry results (PD). Volumes are reported as mean  $\pm$  standard deviation. The  $p$ -values demonstrate the overall differences across population groups as measured using Kruskal Wallis tests.

SDC<sub>NORM</sub> volume: normalized SDC volume

## 2.3 Results

A set of KWTs indicated that for both topographical representations the change in SDC, the change in normalized SDC and diaphragm/costal ratio were significantly affected by population groups. Post-hoc Dunn tests revealed that for the anatomical topographical representation the change in SDC, the change in normalized SDC and diaphragm/costal ratio were lower in Pompe patients with decreased spirometry results than in healthy controls ( $p < 0.001$ ,  $p = 0.001$  &  $p = 0.001$ ) as well as in Pompe patients with normal spirometry results ( $p = 0.004$ ,  $p < 0.001$  &  $p = 0.006$ ). Similar results were found for the functional topographical representation where the change in SDC, the change in normalized SDC and diaphragm/costal ratio were also significantly lower in Pompe patients with decreased spirometry results than in healthy controls ( $p < 0.001$ ,  $p < 0.001$  &  $p = 0.005$ ) and Pompe patients with normal spirometry results ( $p = 0.001$ ,  $p < 0.001$  &  $p = 0.012$ ).

### 2.3.6 Comparison of mesh-derived segmental volumes to PFT outcomes

Table 6 shows the correlation coefficients between several parameters related to the change in diaphragm and costal segmental volume during inspiration and a select subset of measurements obtained from the pulmonary function tests performed prior and during the MRI acquisition.

**Table 6.** Correlations between segmental volume outcomes and pulmonary function test outcomes.

	Topographical representation	VC <sub>mesh</sub>	VC <sub>spiro</sub>	FVC <sub>supine</sub>	FVC <sub>upright</sub>	ΔFVC	MIP	MEP	MEP/MIP
Δ Diaphragm volume	Anatomical	0.943***	0.924***	0.923***	0.799***	-0.686***	0.580***	0.379**	-0.323*
	Functional	0.948***	0.924***	0.925***	0.806***	-0.659***	0.608***	0.402**	-0.326*
Δ Costal volume	Anatomical	0.886***	0.882***	0.879***	0.917***	-0.405**	0.528***	0.478***	-0.089
	Functional	0.730***	0.721***	0.710***	0.793***	-0.253	0.431***	0.457***	0.010
Δ Diaphragm <sub>NORM</sub> volume	Anatomical	0.849***	0.826***	0.810***	0.639***	-0.717***	0.561***	0.327*	-0.368**
	Functional	0.824***	0.795***	0.785***	0.607***	-0.704***	0.565***	0.296*	-0.401**
Δ Costal <sub>NORM</sub> volume	Anatomical	0.716***	0.695***	0.685***	0.550***	-0.521***	0.529***	0.331*	-0.272
	Functional	0.574***	0.555***	0.535***	0.454***	-0.374**	0.443***	0.350*	-0.139
Δ SDC volume	Anatomical	0.980***	0.970***	0.973***	0.926***	-0.586***	0.602***	0.474***	-0.209
	Functional	0.997***	0.971***	0.974***	0.885***	-0.660***	0.645***	0.477***	-0.264
Δ SDC <sub>NORM</sub> volume	Anatomical	0.799***	0.772***	0.763***	0.593***	-0.636***	0.571***	0.348*	-0.321*
	Functional	0.827***	0.796***	0.786***	0.604***	-0.686***	0.579***	0.337*	-0.361**
Δ Diaphragm / Δ Costal ratio	Anatomical	0.593***	0.566***	0.553***	0.381**	-0.645***	0.315*	0.163	-0.260
	Functional	0.535***	0.517***	0.518***	0.351*	-0.596***	0.296*	0.104	-0.298*

The Spearman correlation coefficients  $r_s$  are reported for each combination. The significance level of the correlation coefficients is depicted using the following structure. \*:  $p < 0.05$ , \*\*:  $p < 0.01$ , \*\*\*:  $p < 0.001$ .

Diaphragm<sub>NORM</sub> volume: normalized diaphragm volume, Costal<sub>NORM</sub> volume: normalized costal volume, SDC<sub>NORM</sub> volume: normalized SDC volume, ΔFVC = %FVC<sub>upright</sub> - %FVC<sub>supine</sub>

The best overall correlations were found when comparing the change in SDC volume to the VC<sub>mesh</sub> measurements for both the anatomical ( $r_s = 0.980$ ,  $p < 0.001$ ) and functional ( $r_s = 0.997$ ,  $p < 0.001$ ) topographical representations. Correlations for the change in diaphragm volume were generally better than the correlations for the change in costal diaphragm volume. This was the case for both topographical representations with the exception of the comparisons against the MEP measurements. Here the correlations were better with the change in costal volume than with the change in diaphragm value. Correlations with the pulmonary function test outcomes were better when compared with the changes in segmental volume rather than the changes in normalized segmental volume. Only when compared against ΔFVC did the changes in normalized diaphragm, costal and

## 2.3 Results

SDC volumes provided better significant correlations than their non-normalized counterparts. Out of all segments the change in (normalized) volume of the diaphragm segment correlated best with the drop in  $\Delta FVC$  ( $r_s = -0.717$ ,  $p < 0.001$ ). The negative correlation indicates that the drop in  $\Delta FVC$  was larger for participants that displayed small (or even negative) changes in diaphragm volume than participants with large positive changes in diaphragm volume. MIP measurements provided a better correlation with all segmental volume related outcomes than the MEP measurements. The correlations with the MIP measurements were generally higher for the functional topographical representation than for the anatomical topographical representation except when compared against the change in (normalized) costal volume. The MEP/MIP ratio presented the lowest correlation coefficients when compared against the segmental volume related outcomes and in most cases did not provide a significant correlation.

### 2.3.7 Superoinferior and anteroposterior lung sizes and ratios

Table 7 presents the differences in superoinferior (SI) and anteroposterior (AP) lung sizes between maximal inspiration and maximal expiration as well as the SI and AP ratio for each population group. A significant effect between population groups was found using a KWT for the difference in SI size ( $p < 0.001$ ), SI ratio ( $p < 0.001$ ) and AP ratio ( $p = 0.035$ ). No significant differences between population groups were found for the difference in AP size ( $p > 0.050$ ). Post hoc Dunn tests revealed that the median difference in SI size and median SI ratio were significantly lower in Pompe patients with decreased spirometry results than in healthy controls (both  $p < 0.001$ ) as well as in Pompe patients with normal spirometry results (both  $p < 0.001$ ). A post-hoc Dunn test also revealed that the median AP ratio was significantly higher in Pompe patients with normal spirometry results than in Pompe patients with decreased spirometry results ( $p = 0.031$ ).

**Table 7.** Lung size and ratio outcomes.

	HC	PN	PD	$p$ value
SI size (mm)	60.7 ± 15.45	61.64 ± 9.60	27.61 ± 22.54	<0.001
AP size (mm)	46.93 ± 19.41	53.93 ± 16.32	40.79 ± 16.13	0.090
SI ratio	1.40 ± 0.09	1.41 ± 0.07	1.18 ± 0.15	<0.001
AP ratio	1.32 ± 0.16	1.39 ± 0.14	1.28 ± 0.13	0.035

Results are presented for healthy controls (HC), Pompe patients with normal spirometry results (PN) and Pompe patients with decreased spirometry results (PD). Volumes are reported as mean ± standard deviation. The  $p$ -values demonstrate the overall differences across population groups as measured using Kruskal Wallis tests.

**Table 8.** Correlations between segmental volumes and SI outcomes

	Topographical representation	$\Delta$ SI size	SI ratio
	$\Delta$ Diaphragm volume	Anatomical	0.916***
	Functional	0.917***	0.888***
$\Delta$ Diaphragm <sub>NORM</sub> volume	Anatomical	0.932***	0.936***
	Functional	0.928***	0.934***

The Spearman correlation coefficients  $r_s$  are reported for each combination. All correlation coefficients had a significance level of  $p < 0.001$  as indicated with \*\*\*.  $\Delta$ SI size is the difference in SI size between maximal inspiration and expiration. Diaphragm<sub>NORM</sub> volume: normalized diaphragm volume

### 2.3.8 Comparison of mesh-derived segmental volumes to lung sizes and ratios

The correlation coefficients for the comparison between the change in (normalized) diaphragm volume and the SI outcomes are reported in Table 8. SI size correlated best with the change in non-normalized diaphragm volume while the SI ratio showed a better correlation with the change in normalized diaphragm volume. The correlation coefficients were nearly identical for both topographical representations. All correlations were highly significant ( $p < 0.001$ ).

## 2.3 Results

Table 9 presents the correlations between the change in (normalized) anterior and costal volumes and the AP outcomes. Similar to the results for the correlations with the SI outcomes the AP size correlated best with the change in non-normalized anterior and costal volumes while the AP ratio showed a better correlation with the change in normalized anterior and costal volumes. For the anterior segment the correlations were slightly better in the functional topographical representation than in the anatomical topographical representation. Conversely, for the change in non-normalized costal volume the correlations were actually substantially worse in the functional topographical representation than in the anatomical topographical representation. All correlations were highly significant ( $p < 0.001$ ).

**Table 9.** Correlations between segmental volumes and AP outcomes

	Topographical representation	$\Delta$ AP size	AP ratio
$\Delta$ Anterior volume	Anatomical	0.668***	0.603***
	Functional	0.706***	0.635***
$\Delta$ Costal volume	Anatomical	0.649***	0.565***
	Functional	0.592***	0.475***
$\Delta$ Anterior <sub>NORM</sub> volume	Anatomical	0.717***	0.776***
	Functional	0.734***	0.788***
$\Delta$ Costal <sub>NORM</sub> volume	Anatomical	0.672***	0.712***
	Functional	0.678***	0.706***

The Spearman correlation coefficients  $r_s$  are reported for each combination. All correlation coefficients had a significance level of  $p < 0.001$  as indicated with \*\*\*.  $\Delta$ AP size is the difference in AP size between maximal inspiration and expiration. Anterior<sub>NORM</sub> volume: normalized anterior volume  
Costal<sub>NORM</sub> volume: normalized costal volume

### 2.4 Discussion

In this chapter it has been shown that a mesh model derived from 3D MRI segmentations can be used to obtain greater insights into the function of the diaphragm in patients with Pompe disease. In a large number of Pompe patients the change in diaphragm segmental volume during inspiration was considerably lower than in healthy controls, an indication of diaphragm impairment. The change in diaphragm volume during inspiration showed strong correlations with VC measurements and a moderate correlation with the postural drop in FVC. It also showed a good correlation when compared against outcomes related to the motion of the diaphragm. When coupled with the relative contribution of the diaphragm to the total increase in lung volume during inspiration, the change in diaphragm volume during inspiration appears to be a good indicator of diaphragm impairment.

#### **Evaluating the validity of the functional topographical representation of the segments**

As there are no major inspiratory muscle groups acting on the medial and posterior side of the lungs the change in segmental lung volumes during inspiration and the relative contributions to the total increase in lung volume during inspiration should be minimal, if not negligible, for these segments. For the anatomical representation this is however clearly not the case as there were highly significant differences between population groups for the change in segmental volume and the relative contributions for the medial and posterior segments. Additionally the normalized changes in segmental volume were fairly high, especially for the posterior segment, and not at all inconsequential. The results found in the functional topographical representation on the other hand were much more in line with expectations.

In the original anatomical topographical representation the average differences between groups were in the region of 0.08 and 0.20 L for the medial and posterior segment respectively. For the functional topographical representation the average differences between groups were reduced to around 0.02 L for both segments. Furthermore across all participants the relative contributions to the increase in lung volume during inspiration were much lower on average in the functional topographical representation than the anatomical topographical representation for the medial ( $3.6 \pm 1.5$  % versus  $4.9 \pm 2.4$  %) and posterior ( $3.7 \pm 1.6$  % versus  $16.8 \pm 4.7$  %) segments. Although the relative contribution was also lower for the costal segment ( $53.2 \pm 19.7$  % versus  $64.3 \pm 11.6$  %) in the functional topographical representation than in the anatomical topographical representation, mainly due the decrease in contribution of the lateral segment, the contribution of the diaphragm segment was considerably higher ( $39.5 \pm 20.7$  % versus  $14.0 \pm 6.7$  %). Altogether the diaphragm and costal segments were responsible for  $92.7 \pm 7.9$  % of the increase in lung volume during inspiration for the functional topographical representation, which was a substantial increase on the  $78.3 \pm 5.0$  % for the anatomical topographical representation. As the diaphragm and intercostal muscles are the main inspiratory muscles involved during inspiration it is much more likely that taken together they would be responsible for over 90% of the increase in volume during inspiration. These findings therefore support the original proposition that the functional topographical representation provides a better estimate of the actual underlying muscle function contributions to the increase in lung volume during inspiration.

### Comparing segmental volumes against PFT results

The change in (normalized) segmental volumes during inspiration provided strong correlations with all of the conventionally used spirometry measurements. Correlation coefficients for all segments were higher when compared against  $VC_{\text{mesh}}$  than  $VC_{\text{spiro}}$ , which is in line with previous results from Chapter 1 about the offset in bias between the two VC measurement methods. Both the changes in diaphragm and costal volume provided better correlations with  $FVC_{\text{supine}}$  than for  $FVC_{\text{upright}}$ . This finding was expected as the MRI acquisition was performed in the supine position, which means that the segmental volumes were thus also derived in the supine position. It is therefore no surprise that the segmental volumes correlated better with spirometry measurements made in the same rather than in a different measurement position. A small to moderate negative relationship was found when comparing different segmental volumes against  $\Delta FVC$ , the postural drop in FVC. The largest correlations were found when comparing against the change in diaphragm segmental volumes, an expected finding given that postural drop is commonly used to assess diaphragm function when performing spirometry (Fromageot et al., 2001).

It was also found that there was a small to moderate positive relationship between the changes in segmental volumes and the maximal pressure measurements, in particular the MIP measurements. However, for all segments correlations coefficients were higher when comparing the change in segmental volume with the aforementioned spirometry measurements than for the MIP (and MEP) measurements. This effect is likely due the inherent procedure used to measure MIP. Conventionally MIP measurements are made by performing a forced inspiration maneuver. Therefore the MIP measurements determine the combined strength of all inspiratory muscles, not just the strength of the diaphragm. This is further supported by the finding that the correlations with MIP were best for the summed change in diaphragm and costal segmental volumes. Additionally the MIP measurement procedure can be difficult to perform, especially for the patients with Pompe disease. Therefore low values for MIP in Pompe patients can reflect an impairment of the respiratory muscles but also a poor performance in terms of execution of the forced inspiration maneuver (Pessoa et al., 2014). An alternative to MIP measurements is to make use of a maximal sniff nasal inspiratory pressures (SNIP) instead. A SNIP test is easier to perform (Prigent et al., 2004) and may thus provide more representative values in Pompe patients. Results from SNIP have been shown to correlate well with spirometry results and transdiaphragmatic pressures in Pompe patients (Prigent et al., 2012). Future research should consider the use of SNIP tests in order to provide a more detailed outlook on the function of the diaphragm.

### Interpreting segmental volumes and relative contributions to increase in lung volume

Differences in normalized segmental volumes between population groups were predominantly as a result of differences in normalized segmental inspiratory volumes between population groups. The normalized segmental expiratory volumes were largely equivalent across population groups. A difference was only found for the lateral and medial segments and these differences were sufficiently small (0.02 L) to be inconsequential when assessing the change in normalized segmental volumes between maximal inspiration and maximal expiration.

The change in normalized diaphragm volume during inspiration was considerably lower in Pompe patients with decreased spirometry results than in healthy controls and the remaining Pompe patients. On average, the change in normalized diaphragm volume was around 0.60 L lower in Pompe patients with decreased spirometry results than in the other groups. This was by far the largest difference in change in segment volume between population groups for all segments. The only other segment for which any kind of significant and substantial difference was found between population groups was for the anterior

## 2.4 Discussion

segment, where for the Pompe patients with decreased spirometry results the change in anterior volume during inspiration was on average 0.14 L lower than in the other population groups. However, a significant difference was only found between Pompe patients with decreased spirometry results and Pompe patients with normal spirometry results. These findings again show that the diaphragm segment is the main segment that leads to the differences in inspiratory volume between the population groups and further illustrate the different involvements of the diaphragm and (inter-)costal components during inspiration in Pompe patients. This is further supported by the finding that generally all VC and FVC measurements correlated better with the change in (normalized) diaphragm volume than with the change in (normalized) costal volume, which is another indication that the impact of the diaphragm is the most important factor involved with the change in lung volume during inspiration. Altogether these findings are consistent with results from other studies with patients with Pompe disease (Gaeta et al., 2013; Gaeta et al., 2015; Harlaar et al., 2021). Similar results are however not necessarily found for other muscular disease that can affect the respiratory system, such as Duchenne muscular dystrophy (Barnard et al., 2019). For these patients it was found that both the diaphragm and intercostal muscles were strongly affected by the progression of the disease.



**Figure 21.** A sagittal view of the mesh model of the lungs in three different subjects. Subject 1 is a healthy control, Subject 2 is a Pompe patient with decreased movement of the diaphragm and Subject 3 is a Pompe patients that displays an inverted diaphragm movement (paradoxical breathing). All meshes are depicted in the same orientation and scale.

The relative contributions of the costal and diaphragm segments to the total increase in lung volume during inspiration are fairly consistent for healthy controls and Pompe patients with normal spirometry results, ranging from 35 to 60 % for both segments. For Pompe patients with decreased spirometry results the relative contributions of the costal and diaphragm segments are much more varied across participants. Although on average the relative contribution of the diaphragm was about 22 percent point lower in the group of Pompe patients with decreased spirometry results than the other groups, half of the Pompe patients in this group displayed a similar level of diaphragm contribution as the participants in the other groups. This indicates that not all Pompe patients that presented with decreased spirometry results necessarily also presented with an impairment of the diaphragm. The use of 3D MRI when assessing diaphragm function therefore appears to provide a different level of insight into the function and contribution of the diaphragm during inspiration than conventional spirometry tests.

### **Diaphragm contribution during inspiration for Pompe patients**

With results from the current study as a reference marker, normalized diaphragm volumes were deemed to be lower than normal for increases in volume during inspiration for less than 0.50 L while the relative contribution of the diaphragm to the total increase in lung volume during inspiration was deemed to be less than normal for diaphragm contributions lower than 35%. None of the healthy controls displayed a decreased level of increase in normalized diaphragm volume during inspiration. A group of 16 Pompe patients did present with a decreased level of increase in normalized diaphragm volumes during inspiration. However, while again none of the healthy controls displayed a decreased contribution of the diaphragm during inspiration, only 11 Pompe patients presented with such a decreased contribution of the diaphragm during inspiration. These findings indicate that diaphragm function should not be assessed using only the normalized changes in diaphragm volume. The normalized changes in diaphragm volume should be analyzed in conjunction with the relative contribution of the diaphragm in order to provide a more accurate assessment of diaphragm function and the degree of impairment of the diaphragm.

In the group of 11 Pompe patients that presented with a decreased contribution of the diaphragm during inspiration, three Pompe patients actually displayed a decrease in normalized diaphragm volume during inspiration. These Pompe patients therefore also displayed a negative contribution of the diaphragm to the total increase in lung volume during inspiration. This indicates that for these Pompe patients the diaphragm was impaired to such a severe extent that it actively compromised the participants' ability to increase the volume of the lungs during inspiration.

This raises an important question as to why for some Pompe patients the diaphragm seemingly not just ceases to function properly but actually starts to be a detrimental factor during inspiration. For one Pompe patient in particular the relative contribution of the diaphragm during inspiration was considerably lower (-51.9 %) than for any of the other participants. Further analysis of the results and visual inspection of the mesh model of this Pompe patient may provide an explanation. Figure 21 shows a sagittal view of the lung mesh model for a random healthy control (a), a random Pompe patient with decreased diaphragm motion (b) and the Pompe patient with the considerably large negative contribution of the diaphragm (c). In contrast to the healthy control and the Pompe patient with decreased diaphragm motion the participant depicted in Figure 21c is the only participant that shows an inverted movement of the diaphragm. Conventionally the diaphragm moves downward during inspiration as the diaphragm contracts. However in rare cases the diaphragm can actually move upwards during inspiration. This phenomenon is known as paradoxical diaphragm movement or paradoxical breathing. Paradoxical breathing is typically a sign of severe respiratory muscle dysfunction or weakness (Cahalin et al., 2009). It can be caused by various underlying conditions, such as paralysis of the diaphragm, some obstructive lung diseases (such as COPD and asthma), general muscle weakness or some kind of chest wall abnormalities (such as flail chest or any other type of chest wall trauma). It seems logical that for this participant the most likely cause of paradoxical breathing is a severe weakness of the diaphragm. These findings are supported by the SI size findings. For this participant the difference in SI size between maximal inspiration and maximal expiration was slightly negative (-4.64 mm), which indicates that the apex of the diaphragm was positioned closer to the apex of lungs at maximal inspiration than in maximal expiration. This suggests that the diaphragm moved upwards during the inspiratory maneuver. The occurrence of the paradoxical breathing pattern may explain why this participant in particular demonstrates such a large negative contribution of the diaphragm to the total change in lung volume during inspiration.

### **Comparing segmental volumes against lung size related outcomes**

Differences in superoinferior movement of the diaphragm and superoinferior lung height as well as differences in anteroposterior lung size are often used as an estimate of the contributions of the diaphragm and intercostal muscles during respiration (Gaeta et al., 2015; Harlaar et al., 2021; Wens et al., 2015). In this chapter both the difference in SI size between maximal inspiration and maximal expiration and the SI ratio showed good correlations with the change in (normalized) diaphragm volume during inspiration, indicating that analysis of the diaphragm volume of the mesh model provides similar differences between participants and population groups as the other outcomes based on changes in lung dimensions.

The outcomes based on changes in the AP dimension between maximal inspiration and maximal expiration also showed good correlations with the change in volumes during inspiration of the anterior and costal segments. Interestingly the correlation coefficients for both the AP ratio and change in AP size were higher when compared against the change in volume of the anterior segment than when compared against volume changes of the costal segments. These results were consistent across both the changes in normalized and non-normalized volumes. This finding indicates that differences in the AP dimension were a better predictor of the change in volume during inspiration for the anterior segment than for the costal segment. Whilst the outcomes related to changes in the AP size are still decent predictors of the change in volume of the costal segment during inspiration, it appears that excluding changes in the mediolateral direction from the analysis of the costal contribution to inspiration may substantially alter the determined outcomes. The current research therefore also highlights the importance of incorporating changes in the mediolateral direction in the analysis of the respiratory mechanics. In a previous study Wens et al. (2015) found no difference in mediolateral length ratios in the lungs between healthy controls and Pompe patients. However in the current research small but significant differences in the contributions of the lateral and medial segments to the total change in lung volume were found in the functional topographical representation of the segments between healthy controls and Pompe patients. These differences were especially prominent for the lateral segment, with an average contribution to the total increase in lung volume during inspiration of  $7.9 \pm 5.4$  % across all participants. Altogether 15 % of the total contribution of the costal segment to the increase in lung volume during inspiration was comprised of the contribution of the lateral segment. The change in volume of the entire costal segment therefore appears to not just be dependent on the movement of the rib cage in the anteroposterior but also in the mediolateral direction. This also emphasizes a large advantage of the use of 3D imaging over 2D imaging. 3D imaging can readily be used to assess changes along all three main axes of the 3D MRI acquisition, while for 2D imaging it can be very difficult to properly quantify the movement of the costal segment in both the anteroposterior and mediolateral directions while still being able to quantify the displacement of the diaphragm in the superoinferior direction.

## 2.5 Conclusion

In this chapter it was shown that the use of a mesh model derived from 3D MRI data provided valuable insights into the function of the diaphragm in Pompe patients. It was demonstrated that transforming the allocation of the segmental volumes based on the dimension changes during inspiration provided a more sensible functional topographical representation of the actual contribution of the underlying muscle functions during inspiration. The resulting segmental volumes showed good correlations with existing outcomes used to assess the diaphragm function, such as spirometry measurements and displacement of the diaphragm. It was demonstrated that the change in segmental volumes during inspiration could be used in conjunction with the relative contribution of the segments to the total increase in lung volume to provide a detailed assessment of diaphragm function in Pompe patients. In a large number of patients with Pompe disease the change in diaphragm segmental volume during inspiration was considerably lower than in healthy controls, indicating an impairment of the diaphragm function. It was also discovered that for some Pompe patients with decreased spirometry results no apparent decrease in the contribution of the diaphragm during inspiration was found. These findings suggest that a mesh model can be used as a valuable and beneficial tool alongside conventional spirometry measurements to provide a more accurate assessment of diaphragm impairment in patients with Pompe disease.

# General discussion

In this study static breath-hold 3D MRI segmentations have been used to create an anatomically accurate mesh model of the lungs. VC measurements retrieved from the mesh models showed good correlation with VC measurements obtained spirometry. Although the VC measurements retrieved from the mesh models were generally slightly lower than the spirometry VC measurements, this offset was inconsequential for the analysis of the segmental volumes in the mesh model. Differences in segmental volumes between meshes generated at maximal inspiration and maximal expiration were assessed for healthy controls and Pompe patients. It has been demonstrated that changes in diaphragm volume and the relative contribution of the diaphragm to the total increase in lung volume during inspiration were decreased in some patients with Pompe disease. Changes in diaphragm volumes correlated well with conventional VC and FVC measurements as well as with changes in superoinferior lung sizes, a measurement typically used in 2D analysis of the diaphragm and lungs. In some Pompe patients with decreased spirometry results no indication for diaphragm impairment was found when assessing the relative contribution of the diaphragm to the total increase in lung volume. These results indicate that a MRI-based mesh model may provide valuable additional information about the function of the diaphragm in Pompe patients.

### Study limitations

The main limitation of the current study is the need for multiple repair algorithms in order to ensure that an anatomically correct mesh model could be generated for all participants. In some cases the underlying random walker algorithm was unable to properly identify the medial region of the lung surface. Due to large inter-subject variations in lung shapes the repair algorithms could not be applied to the mesh automatically. When repair algorithms were applied to a mesh model that was already anatomically correct the feature labeling process could result in incorrectly labeled mesh structures. Therefore using the current pipeline requires the user to visually inspect the mesh model and if necessary select the required repair algorithms. Although manual visual inspection of the meshes is generally always recommended, this means that the current pipeline cannot be used to generate the mesh models fully automatically without additional user input.

Another limitation of the current outlined pipeline is that it requires two separate static 3D segmentations at maximal inspiration and maximal expiration. These static 3D scans are collected during a breath-hold procedure. Although the acquisition time for each slice is relatively short, this procedure can prove challenging for Pompe patients with severe diaphragm weakness. The segmentations of the original static 3D scans were generated using a currently unreleased proof-of-concept script that generates the 3D segmentations automatically. Furthermore, the current pipeline can only be applied to static 3D segmentations unlike the original paper by Mogalle et al. (2016). In their described pipeline the mesh could also be propagated over time using dynamic 3D MRI, hereby generating multiple mesh models that depict different stages of respiration.

Lastly it is important to note that the mesh model of the lungs generated using the current pipeline can only be used to identify the portion of the diaphragm that directly connects to the lungs. The current method can therefore not be used to visualize the entire diaphragm. For the current study this did not cause any problems as the mesh model was essentially used to assess the function of the diaphragm through the effect of the movement of diaphragm on the lungs.

### Future research

The mesh model based on 3D MRI outlined in the current study is a versatile tool that can be used to assess a large number of variables related to the respiratory function. A powerful advantage of the current mesh model is that once generated the mesh structure can readily be used for future research into other aspects identifiable in the mesh model. One of these aspects is the curvature of the diaphragm. Previous research found that the curvature of the diaphragm was different in patients with Pompe disease, even in patients with normal spirometry results (Harlaar et al., 2021). Other studies have also reported that the shape of the diaphragm may be a strong indicator of diaphragm impairment, with the posterior side of the diaphragm showing greater displacement than the anterior side of the diaphragm in supine (Mogalle et al., 2016) and upright (Takazakura et al., 2004) positions. In the current study there was no indication of a substantial difference in diaphragm function between healthy controls and Pompe patients with normal spirometry results. A future study that aims to assess the curvature of the diaphragm using the current mesh model may be able to provide even greater insight into the function of the diaphragm and perhaps allow for earlier identification of diaphragm impairment.

The mesh labeling algorithm contained within the current pipeline ensures that visual inspection is required after the generation of the mesh due to the repair algorithms that may have to be applied to the mesh model. These repair algorithms are necessary because the main labeling algorithm of the current pipeline is based on the random walker algorithm. This algorithm performs poorly in the absence of clear boundaries between segments in the mesh structure. Furthermore, the random walker algorithm is fairly time-intensive as it iteratively changes assigned labels of the mesh structure. Other algorithms, such as shape matching and machine learning algorithms, may be considered as alternatives for the current random walker algorithm. Such algorithms could prove to be highly useful in accurately identifying the concave regions of the lung surface (i.e. the medial and diaphragmatic surfaces) and may eliminate the need for additional repair algorithms, thereby automating the entire mesh generation process and likely reducing the overall mesh generation time. Implementing these algorithms may prove to be difficult due to the high inter-subject variability in the shape of the lungs, but it may be worth exploring whether such algorithms can efficiently be applied to the current pipeline.

For future studies a consideration should also be made to compare outcomes measures in Pompe patients against SNIP measurements instead of MIP and MEP measurements. Results from SNIP tests correlate well with spirometry results and transdiaphragmatic pressures in patients with Pompe disease (Prigent et al., 2012). Transdiaphragmatic pressures have previously been shown to be a good indicator of diaphragm muscle strength in Pompe patients (Smith et al., 2016). SNIP tests should be easier to perform for Pompe patients than the often-strenuous MIP tests and are therefore more likely to provide representative results of the strength and function of the diaphragm.

In the current study differences between population groups were only assessed using a cross-sectional design. For a future study a longitudinal approach may be considered to determine whether the current mesh model can be used to assess differences in Pompe patients over a longer period of time. This would provide vital information into the capabilities of the current method to identify a deterioration of diaphragm function over time. A longitudinal study design using the current mesh model should not be overly complicated given that the MRI acquisition procedure for the breath-hold MRI is fairly straightforward. Additional spirometry tests would not necessarily be required in order to assess the validity of the mesh models.

Lastly, it is important that MRI scans are performed in a large population of healthy subjects in order to obtain a large database of future reference values. These reference values are essential when assessing abnormal results in Pompe patients and/or patients with other respiratory diseases or deficiencies. Additionally a large number of available datasets is potentially also well suited to be combined with a machine learning model. By training and validating the machine learning model with a large number of datasets we can help ensure that the model can generalize to new data, hereby generating a more accurate mesh model of the lungs.

### **Overall conclusion**

In the current study we demonstrated that the use of a mesh model based on static breath-hold 3D MRI segmentations is a versatile tool in assessing diaphragm function. Whilst results from spirometry tests provide a good indication of diaphragm weakness, we have shown that a mesh model can be used to provide valuable information about specific aspects of the impairment of the diaphragm that a conventional spirometry test cannot provide. More accurate detection and estimation of diaphragm impairment may aid in optimizing the effectiveness of treatments for Pompe patients. Further research into other outcomes such as the curvature of the diaphragm may provide even more valuable information about the function of the diaphragm.

## References

- Alejaldre, A., Díaz-Manera, J., Ravaglia, S., Tibaldi, E. C., D'Amore, F., Morís, G., ... & Pichiecchio, A. (2012). Trunk muscle involvement in late-onset Pompe disease: study of thirty patients. *Neuromuscular Disorders*, 22, S148-S154.
- Archip, N., Rohling, R., Dessenne, V., Erard, P. J., & Nolte, L. P. (2006). Anatomical structure modeling from medical images. *Computer Methods and Programs in Biomedicine*, 82(3), 203-215.
- Attene, M. (2010). A lightweight approach to repairing digitized polygon meshes. *The visual computer*, 26, 1393-1406.
- Ausems, M. G. E. M., Verbiest, J., Hermans, M. M. P., Kroos, M. A., Beemer, F. A., Wokke, J. H. J., ... & Van der Ploeg, A. T. (1999). Frequency of glycogen storage disease type II in The Netherlands: implications for diagnosis and genetic counselling. *European Journal of Human Genetics*, 7(6), 713-716.
- Bade, R., Haase, J., & Preim, B. (2006, March). Comparison of fundamental mesh smoothing algorithms for medical surface models. In *SimVis*, 6, 289-304.
- Bakker, J. T., Klooster, K., Bouwman, J., Pelgrim, G. J., Vliegenthart, R., & Slebos, D. J. (2022). Evaluation of spirometry-gated computed tomography to measure lung volumes in emphysema patients. *ERJ Open Research*, 8(1), 1-12.
- Barba-Romero, M. A., Barrot, E., Bautista-Lorite, J., Gutierrez-Rivas, E., Illa, I., Jimenez, L. M., ... & Vilchez-Padilla, J. J. (2012). Clinical guidelines for late-onset Pompe disease. *Rev Neurol*, 54(8), 497-507.
- Barnard, A. M., Lott, D. J., Batra, A., Triplett, W. T., Forbes, S. C., Riehl, S. L., ... & Walter, G. A. (2019). Imaging respiratory muscle quality and function in Duchenne muscular dystrophy. *Journal of neurology*, 266(11), 2752-2763.
- Barreiro, T., & Perillo, I. (2004). An approach to interpreting spirometry. *American family physician*, 69(5), 1107-1114.
- Barros, R., Raposo, L., Moreira, N., Rocha, M., Calaça, P., Spencer, I., ... & Norte, C. H. U. L. (2021). Slow Vital Capacity: Differences Between the Expiratory Vital Capacity and the Inspiratory Vital Capacity. *Revista Americana de Medicina Respiratoria*, 21(2), 177-186.
- Cacciola, F., Rouxel-Labbé, M., and Senbaşlar, B. (n.d.) CGAL 5.5.2 - Triangulated Surface Mesh Simplification. Retrieved June 18, 2023, from [https://doc.cgal.org/latest/Surface\\_mesh\\_simplification/index.html](https://doc.cgal.org/latest/Surface_mesh_simplification/index.html)
- Cahalin, L. P., Braga, M., Matsuo, Y., & Hernandez, E. D. (2002). Efficacy of diaphragmatic breathing in persons with chronic obstructive pulmonary disease: a review of the literature. *Journal of Cardiopulmonary Rehabilitation and Prevention*, 22(1), 7-21.
- Carlier, R. Y., Laforet, P., Wary, C., Mompoin, D., Laloui, K., Pellegrini, N., ... & Orlikowski, D. (2011). Whole-body muscle MRI in 20 patients suffering from late onset Pompe disease: Involvement patterns. *Neuromuscular Disorders*, 21(11), 791-799.
- Celli, B. R. (2000). The importance of spirometry in COPD and asthma: effect on approach to management. *Chest*, 117(2), 15S-19S.
- Chaudhry R. & Bordoni B. (2022) Anatomy, Thorax, Lungs. In: StatPearls [Internet]. *StatPearls Publishing*. Available from: <https://www.ncbi.nlm.nih.gov/books/NBK470197/>
- Crescimanno, G., Palazzolo, L., Bertini, M., Arriscato, S., & Marrone, O. (2021). Long-term evaluation of respiratory outcomes in patients with late onset Pompe disease under enzyme replacement therapy: the role of postural drop and its impact on quality of life. *European Respiratory Journal*, 58, 1-5.
- Criée, C. P., Soricther, S., Smith, H. J., Kardos, P., Merget, R., Heise, D., ... & Mitfessel, H. (2011). Body plethysmography—its principles and clinical use. *Respiratory medicine*, 105(7), 959-971.

## References

---

- Cupler, E. J., Berger, K. I., Leshner, R. T., Wolfe, G. I., Han, J. J., Barohn, R. J., ... & AANEM CONSENSUS COMMITTEE ON LATE-ONSET POMPE DISEASE. (2012). Consensus treatment recommendations for late-onset Pompe disease. *Muscle & nerve*, 45(3), 319-333.
- De Troyer, A., & Boriek, A. M. (2011). Mechanics of the respiratory muscles. *Comprehensive Physiology*, 1(3), 1273-1300.
- Fang, Q., & Boas, D. A. (2009, June). Tetrahedral mesh generation from volumetric binary and grayscale images. In 2009 *IEEE international symposium on biomedical imaging: from nano to macro*, 1142-1145.
- Figueroa-Bonaparte, S., Segovia, S., Llauger, J., Belmonte, I., Pedrosa, I., Alejaldre, A., ... & Spanish Pompe Study Group. (2016). Muscle MRI findings in childhood/adult onset Pompe disease correlate with muscle function. *PLoS one*, 11(10), e0163493.
- Fromageot, C., Lofaso, F., Annane, D., Falaize, L., Lejaille, M., Clair, B., ... & Raphaël, J. C. (2001). Supine fall in lung volumes in the assessment of diaphragmatic weakness in neuromuscular disorders. *Archives of physical medicine and rehabilitation*, 82(1), 123-128.
- Gaeta, M., Barca, E., Ruggeri, P., Minutoli, F., Rodolico, C., Mazziotti, S., ... & Toscano, A. (2013). Late-onset Pompe disease (LOPD): correlations between respiratory muscles CT and MRI features and pulmonary function. *Molecular genetics and metabolism*, 110(3), 290-296.
- Gaeta, M., Musumeci, O., Mondello, S., Ruggeri, P., Montagnese, F., Cucinotta, M., ... & Toscano, A. (2015). Clinical and pathophysiological clues of respiratory dysfunction in late-onset Pompe disease: New insights from a comparative study by MRI and respiratory function assessment. *Neuromuscular Disorders*, 25(11), 852-858.
- Grady, L. (2006). Random walks for image segmentation. *IEEE transactions on pattern analysis and machine intelligence*, 28(11), 1768-1783.
- Graham, B. L., Steenbruggen, I., Miller, M. R., Barjaktarevic, I. Z., Cooper, B. G., Hall, G. L., ... & Thompson, B. R. (2019). Standardization of spirometry 2019 update. An official American thoracic society and European respiratory society technical statement. *American journal of respiratory and critical care medicine*, 200(8), 70-88.
- Guéziec, A., Taubin, G., Lazarus, F., & Hom, B. (2001). Cutting and stitching: Converting sets of polygons to manifold surfaces. *IEEE Transactions on Visualization and Computer Graphics*, 7(2), 136-151.
- Johns, D. P., Walters, J. A., & Walters, E. H. (2014). Diagnosis and early detection of COPD using spirometry. *Journal of thoracic disease*, 6(11), 1557-1569.
- Levine, J. A., Paulsen, R. R., & Zhang, Y. (2012). Mesh Processing in Medical-Image Analysis—a Tutorial. *IEEE computer graphics and applications*, 32(5), 22-28.
- Lindstrom, P., & Turk, G. (1998). Fast and memory efficient polygonal simplification. In *Proceedings Visualization'98 (Cat. No. 98CB36276)*. IEEE, 279-286.
- Lindstrom, P., & Turk, G. (1999). Evaluation of memoryless simplification. *IEEE Transactions on Visualization and Computer Graphics*, 5(2), 98-115.
- McCool, F. D., & Tzelepis, G. E. (2012). Dysfunction of the diaphragm. *New England Journal of Medicine*, 366(10), 932-942.
- Mellies, U., Ragette, R., Schwake, C., Baethmann, M., Voit, T., & Teschler, H. (2001). Sleep-disordered breathing and respiratory failure in acid maltase deficiency. *Neurology*, 57(7), 1290-1295
- Mogalle, K., Perez-Rovira, A., Ciet, P., Wens, S. C., van Doorn, P. A., Tiddens, H. A., ... & de Bruijne, M. (2016). Quantification of diaphragm mechanics in Pompe disease using dynamic 3D MRI. *PLoS One*, 11(7), e0158912.
- Parthasarathy, S., Jubran, A., Laghi, F., & Tobin, M. J. (2007). Sternomastoid, rib cage, and expiratory muscle activity during weaning failure. *Journal of applied physiology*, 103(1), 140-147.

## References

---

- Pellegrini, N., Laforet, P., Orlikowski, D., Pellegrini, M., Caillaud, C., Eymard, B., ... & Lofaso, F. (2005). Respiratory insufficiency and limb muscle weakness in adults with Pompe's disease. *European Respiratory Journal*, 26(6), 1024-1031.
- Pessoa, I., Schlauser, M. B., Parreira, V. F., Fregonezi, G. A., Sheel, A. W., Chung, F., & Reid, W. D. (2014). Reference values for maximal inspiratory pressure: a systematic review. *Canadian Respiratory Journal*, 21(1), 43-50.
- Prigent, H., Lejaille, M., Falaize, L., Louis, A., Ruquet, M., Fauroux, B., ... & Lofaso, F. (2004). Assessing inspiratory muscle strength by sniff nasal inspiratory pressure. *Neurocritical care*, 1, 475-478.
- Prigent, H., Orlikowski, D., Laforêt, P., Letilly, N., Falaize, L., Pellegrini, N., ... & Lofaso, F. (2012). Supine volume drop and diaphragmatic function in adults with Pompe disease. *European Respiratory Journal*, 39(6), 1545-1546.
- Pottmann, H., Steiner, T., Hofer, M., Haider, C., & Hanbury, A. (2004). The isophotic metric and its application to feature sensitive morphology on surfaces. In *Computer Vision-ECCV 2004: 8th European Conference on Computer Vision, Prague, Czech Republic, May 11-14, 2004. Proceedings (4)*8, 560-572.
- Quinn, M., St Lucia, K., & Rizzo, A. (2017). Anatomy, anatomic dead space. In: StatPearls [Internet] *StatPearls Publishing*. Available from: <https://www.ncbi.nlm.nih.gov/books/NBK442016/>
- Ruggeri, P., Lo Monaco, L., Musumeci, O., Tavilla, G., Gaeta, M., Caramori, G., & Toscano, A. (2020). Ultrasound assessment of diaphragm function in patients with late-onset Pompe disease. *Neurological Sciences*, 41, 2175-2184.
- Schneider, I., Hanisch, F., Müller, T., Schmidt, B., & Zierz, S. (2012). Respiratory function in late-onset Pompe disease patients receiving long-term enzyme replacement therapy for more than 48 months. *Wiener Medizinische Wochenschrift*, 163(1-2), 40-44.
- Shirly, S., & Ramesh, K. (2019). Review on 2D and 3D MRI image segmentation techniques. *Current Medical Imaging*, 15(2), 150-160.
- Smith, B. K., Corti, M., Martin, A. D., Fuller, D. D., & Byrne, B. J. (2016). Altered activation of the diaphragm in late-onset Pompe disease. *Respiratory physiology & neurobiology*, 222, 11-15.
- Stockton, D. W., Kishnani, P., van der Ploeg, A., Llerena, J., Boentert, M., Roberts, M., ... & Berger, K. I. (2020). Respiratory function during enzyme replacement therapy in late-onset Pompe disease: longitudinal course, prognostic factors, and the impact of time from diagnosis to treatment start. *Journal of Neurology*, 267, 3038-3053.
- Takazakura, R., Takahashi, M., Nitta, N., & Murata, K. (2004). Diaphragmatic motion in the sitting and supine positions: healthy subject study using a vertically open magnetic resonance system. *Journal of Magnetic Resonance Imaging: An Official Journal of the International Society for Magnetic Resonance in Medicine*, 19(5), 605-609.
- Tantucci, C., Bottone, D., Borghesi, A., Guerini, M., Quadri, F., & Pini, L. (2016). Methods for measuring lung volumes: is there a better one?. *Respiration*, 91(4), 273-280.
- Taubin, G. (1995, September). A signal processing approach to fair surface design. In *Proceedings of the 22nd annual conference on Computer graphics and interactive techniques*, 351-358.
- Tran, A. P., Yan, S., & Fang, Q. (2020). Improving model-based functional near-infrared spectroscopy analysis using mesh-based anatomical and light-transport models. *Neurophotonics*, 7(1), 015008.
- Van der Beek, N. A. M. E., Van Capelle, C. I., Van der Velden-van Etten, K. I., Hop, W. C. J., van den Berg, B., Reuser, A. J. J., ... & Stam, H. (2011). Rate of progression and predictive factors for pulmonary outcome in children and adults with Pompe disease. *Molecular genetics and metabolism*, 104(1-2), 129-136.
- van den Hout, H. M., Hop, W., van Diggelen, O. P., Smeitink, J. A., Smit, G. P. A., Poll-The, B. T. T., ... & van der Ploeg, A. T. (2003). The natural course of infantile Pompe's disease: 20 original cases compared with 133 cases from the literature. *Pediatrics*, 112(2), 332-340.

## References

---

- Walter, S. S., Fritz, B., Kijowski, R., & Fritz, J. (2023). 2D versus 3D MRI of osteoarthritis in clinical practice and research. *Skeletal Radiology*, 1-14.
- Zhang, J., Zheng, J., & Cai, J. (2010). Interactive mesh cutting using constrained random walks. *IEEE Transactions on Visualization and Computer Graphics*, 17(3), 357-367.
- Zhang, C., & Chen, T. (2001). Efficient feature extraction for 2D/3D objects in mesh representation. *In Proceedings 2001 International Conference on Image Processing (Cat. No. 01CH37205 (3))*, 935-938.

# Appendix A – Mesh VC compared against spirometry FVC

The VC as retrieved from the mesh model was also compared against spirometry FVC measurements made in the supine position prior to the MRI acquisition (Figure 22). Although there was no significant difference between median VC and FVC spirometry measurements ( $p = 0.241$ ), the difference with  $VC_{\text{mesh}}$  was on average 0.17 L higher when compared with FVC measurement than when compared with the spirometry VC measurements. Across all population groups FVC was higher than  $VC_{\text{mesh}}$  ( $p < 0.001$ ) with an average difference of 0.48 L.

The difference in FVC and VC spirometry measurements can likely be explained by the maneuver that was used to determine both outcomes. The FVC measurements were obtained during a standard forced inspiration maneuver, while the spirometry VC measurement were obtained during the breath-hold maneuver performed during the MRI acquisition. During the breath-hold maneuver the main objective for the participants is to maintain the requested lung volume levels. It is therefore unlikely that participants are able to obtain true TLC and RV values in a breath-hold maneuver, while these should generally be achieved during a standard forced inspiration maneuver. This highlights the importance of using simultaneous measurements when comparing lung volumes across different measurement methods in order to minimize the effects of differences during the execution of successive breathing exercises.

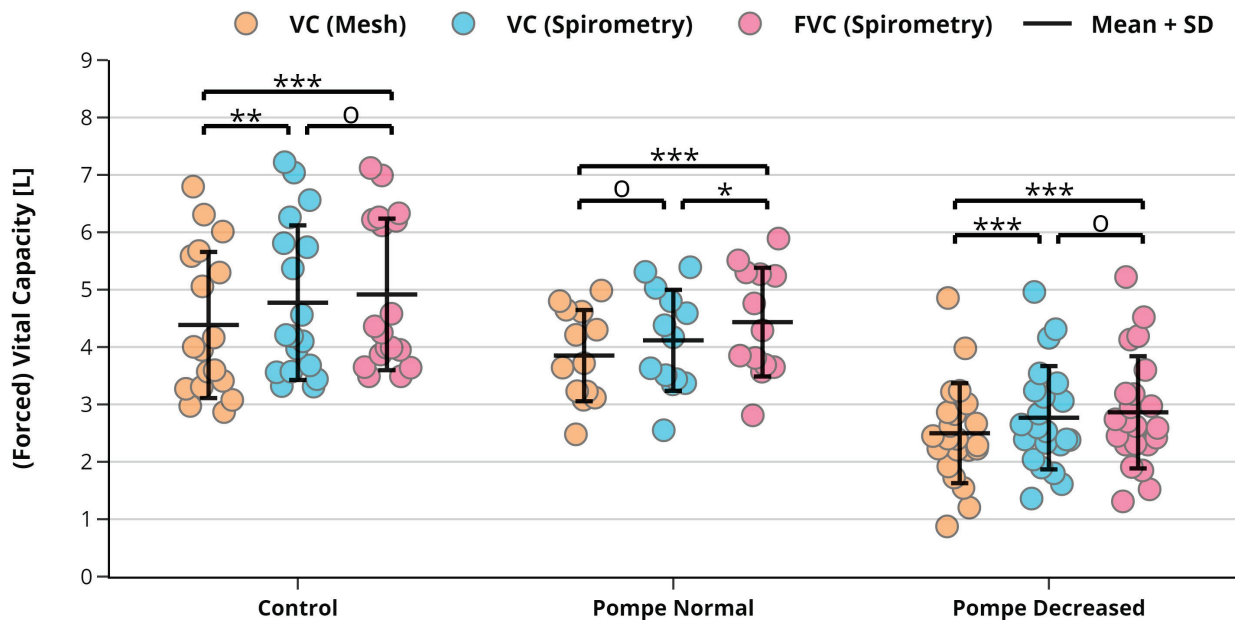


**Figure 22.** A comparison of (forced) vital capacity (FVC/VC) measurements. The VC as retrieved from the mesh is compared against spirometry VC measurements made during the MRI acquisition and the supine FVC measurements made prior to the MRI acquisition for each population group. The data for each individual participant is shown as a filled circle with the mean  $\pm$  standard deviation in the centers of the data.

○ : ns, \* :  $p < 0.05$ , \*\* :  $p < 0.01$ , \*\*\* :  $p < 0.001$ . Control: Healthy controls, Pompe Normal: Pompe patients with normal spirometry results, Pompe Decreased: Pompe patients with decreased spirometry results.